Published online 12 July 2017 *Nucleic Acids Research, 2017, Vol. 45, No. 16* ***9741–9759***
doi: 10.1093/nar/gkx604

A novel non-canonical PIP-box mediates PARG interaction with PCNA

Tanja Kaufmann[1], Irina Grishkovskaya[2], Anton A. Polyansky[2], Sebastian Kostrhon[1], Eva Kukolj[1], Karin M. Olek[1], Sebastien Herbert[1], Etienne Beltzung[1], Karl Mechtler[3], Thomas Peterbauer[1], Josef Gotzmann[4], Lijuan Zhang[5], Markus Hartl[6], Bojan Zagrovic[2], Kareem Elsayad[5], Kristina Djinovic-Carugo[2,7] and Dea Slade[1,*]

[1]Department of Biochemistry, Max F. Perutz Laboratories, University of Vienna, Vienna Biocenter (VBC), Dr. Bohr-Gasse 9, 1030 Vienna, Austria, [2]Department of Structural and Computational Biology, Max F. Perutz Laboratories, University of Vienna, Vienna Biocenter (VBC), Campus Vienna Biocenter 5, 1030 Vienna, Austria, [3]Institute of Molecular Pathology, Vienna Biocenter (VBC), Dr. Bohr-Gasse 7, 1030 Vienna, Austria, [4]Department of Medical Biochemistry, Max F. Perutz Laboratories, Medical University of Vienna, Vienna Biocenter (VBC), Dr. Bohr-Gasse 9, 1030 Vienna, Austria, [5]VBCF-Advanced Microscopy, Vienna Biocenter (VBC), Dr. Bohr-Gasse 3, 1030 Vienna, Austria, [6]Mass Spectrometry Facility, Max F. Perutz Laboratories, Vienna Biocenter (VBC), Dr. Bohr-Gasse 3, 1030 Vienna, Austria and [7]Department of Biochemistry, Faculty of Chemistry and Chemical Technology, University of Ljubljana, Večna pot 113, 1000 Ljubljana, Slovenia

Received March 21, 2017; Revised June 14, 2017; Editorial Decision July 01, 2017; Accepted July 04, 2017

ABSTRACT

Poly(ADP-ribose) glycohydrolase (PARG) regulates cellular poly(ADP-ribose) (PAR) levels by rapidly cleaving glycosidic bonds between ADP-ribose units. PARG interacts with proliferating cell nuclear antigen (PCNA) and is strongly recruited to DNA damage sites in a PAR- and PCNA-dependent fashion. Here we identified PARG acetylation site K409 that is essential for its interaction with PCNA, its localization within replication foci and its recruitment to DNA damage sites. We found K409 to be part of a non-canonical PIP-box within the PARG disordered regulatory region. The previously identified putative N-terminal PIP-box does not bind PCNA directly but contributes to PARG localization within replication foci. X-ray structure and MD simulations reveal that the PARG non-canonical PIP-box binds PCNA in a manner similar to other canonical PIP-boxes and may represent a new type of PIP-box. While the binding of previously described PIP-boxes is based on hydrophobic interactions, PARG PIP-box binds PCNA via both stabilizing hydrophobic and fine-tuning electrostatic interactions. Our data explain the mechanism of PARG–PCNA interaction through a new PARG PIP-box that exhibits non-canonical sequence properties but a canonical mode of PCNA binding.

INTRODUCTION

Poly(ADP-ribosylation) (PARylation) is a post-translational modification synthesized by poly(ADP-ribose) polymerases (PARPs) from NAD. PARylation regulates diverse cellular functions including DNA replication and repair, chromatin remodeling, transcription, cell cycle progression, mitosis, apoptosis, development, differentiation and aging (1–4). PARylation has multiple roles in the DNA damage response: it modulates chromatin structure to enable access to DNA repair factors; it serves as a docking site for PAR-binding proteins involved in chromatin remodeling, DNA repair or transcription regulation; it also determines cell fate depending on the extent of DNA damage (5). Excessive PARylation leads to cell death; hence PAR levels need to be tightly regulated by PARG (6).

In mammalian cells, the addition of PAR is controlled by the action of several PARPs (PARP1–5), whereas its removal is catalyzed mainly by poly(ADP-ribose) glycohydrolase (PARG), which cleaves glycosidic ribose–ribose bonds within PAR chains (7). Human PARG is a 111 kDa protein ($PARG^{111}$) that localizes in the nucleus, while shorter isoforms without the nuclear localization signal (NLS) show cytoplasmic ($PARG^{102}$ and $PARG^{99}$) or mitochondrial ($PARG^{60}$) localization (8). Vertebrate PARG architecture comprises two distinct components: a disordered N-terminal regulatory domain (M1-E460 in hPARG) and a C-terminal catalytic domain (9). The structure of the catalytic domain showed that PARG harbors a macro domain as

*To whom correspondence should be addressed. Tel: +431427752811; Fax: +43142779240; Email: dea.slade@univie.ac.at

an ADP-ribose binding module and a PARG-specific loop with conserved glutamates (E755 and E756 in hPARG) required for catalytic cleavage of ribose-ribose bonds (10,11) in an exo-glycohydrolase mode (12).

The PARG regulatory region contains a putative PCNA-interacting protein motif (PIP-box; Q76-W82) (13). Canonical PIP-boxes are defined by the consensus sequence **Q**-x-x-**h**-x-x-**a**-**a**, where '*h*' and '*a*' represent hydrophobic (ILM) and aromatic (FY) amino acids, respectively (14). PCNA is the major coordinator of faithful and processive replication and DNA repair at replication forks (15). The putative PIP-box has been reported to be essential for PARG co-localization with PCNA in S-phase replication foci, although mutation of the PIP-box residues does not affect PARG–PCNA co-immunoprecipitation (13). PARG is strongly recruited to laser-induced DNA damage sites via PAR- and PCNA-dependent pathways (13).

Here, we undertake an integrated biochemical, biophysical, structural, advanced microscopy and mass spectrometry approach to investigate the regulation of PARG by acetylation and the mechanism of PARG–PCNA interaction. We discovered that an acetylated residue, K409, is essential for PARG–PCNA interaction as part of a novel non-canonical PIP-box. The in-depth characterization of the K409-mediated interaction with PCNA via X-ray crystallography, molecular dynamics (MD) simulations, isothermal titration calorimetry (ITC), co-immunoprecipitation and FLIM-FRET showed that both the aliphatic part of the K409 side chain and its positive charge are essential for efficient PCNA binding *in vitro* and *in vivo* and that acetylation negatively regulates PARG–PCNA interaction *in vitro*. While K409 mutation did not affect PARG catalytic activity, chromatin binding or cell-cycle distribution, the K409 residue emerged as the critical regulator of PARG localization within S-phase replication foci and PARG recruitment to laser-induced DNA damage sites.

MATERIALS AND METHODS

Cell lines

Cell lines were maintained in Dulbecco's Modified Eagle's Medium (DMEM 4.5 g/l glucose) (Sigma) supplemented with 10% fetal bovine serum (Sigma), 1% L-glutamine (Sigma), 1% penicillin–streptomycin (Sigma) under 5% CO_2 at 37°C. HEK293T cells were used for transient transfections. U2OS cells were used for microscopy. Stable PARG knockdown (shPARG) and control (shCTRL) HeLa cell lines were maintained in 125 μg/ml hygromycin B (Invivogen) as described previously (16). Transfections were performed with polyethylenimine (PEI; Polysciences).

Plasmids, proteins and peptides

pDONR221 human PARG was from Ivan Ahel (University of Oxford). PARG was transferred into Gateway destination vectors pDEST C-YFP (from Dragana Ahel, University of Oxford) and pDEST C-EGFP (from Daniel Gerlich, IMBA, Vienna). CMV N3xFLAG PARG was obtained by cloning human PARG into CMV10 (Sigma) between NotI and XbaI. PARG truncation mutants (1–75aa, 1–89aa, 1–469aa, 88–469, 88–976aa and 478–976aa) were cloned into pDONR221 and transferred into pDEST C-YFP and pDEST N3xFLAG. shRNA-resistant CMV N3XFLAG PARG was obtained by introducing four silent mutations in the region targeted by shRNA (5′-gaccacaatgagtgcctc-3′). Site-directed mutagenesis was performed with the Phusion polymerase (NEB) according to the FastCloning protocol (17). CBP-myc was from Raul Mostoslavsky, p300-HA (pCMVbeta), FLAG-hMOF, FLAG-PCAF and FLAG-Tip60 (pcDNA3.1) were from Michael Potente, mRFP–PCNA was from Cristina Cardoso (18). hMOF, PCAF and Tip60 were cloned into pDONR221 (Life Technologies) and transferred into pDEST myc (Life Technologies). Human PCNA (Uniprot ID P12004) was obtained from MGC (GE Dharmacon) and cloned into pACE-NH between BsaI sites with an N-terminal his_6 tag and an HRV 3C cleavage site. His_6-PCNA was expressed in *Escherichia coli* Rosetta2 (DE3) cells (Novagen) and purified on HisTrap HP column (GE Healthcare). Following overnight cleavage of his_6 using GST-HRV 3C, PCNA was reloaded onto HisTrap HP column. Flowthrough containing PCNA was loaded onto Superdex 200 (GE Healthcare). Cleaved PCNA used for crystallization contains an extra sequence at the N-terminus: GPAMRP. The regulatory region of PARG (1–447aa) was cloned into pETM11 between NcoI and XhoI with an N-terminal his_6 tag and a TEV cleavage site, expressed and purified as described for PCNA with the exception of overnight cleavage of his_6-TEV-PARG using his_6-TEV. PARG peptides were synthesized by Fmoc solid phase peptide synthesis (SPPS) and purified by reversed phase HPLC (RP-HPLC) (Mathias Madalinski, IMP, Vienna) or purchased from Eurogentec.

Antibodies

The following antibodies were used for Western blotting: anti-FLAG M2-peroxidase clone M2 (1:10 000; Sigma), mouse anti-FLAG M2 (1:5000; Sigma), mouse anti-HA.11 clone 16B12 (1:1000; Covance), mouse anti-myc clone 4A6 (1:1000; Merck Millipore), rabbit anti-acetylated-lysine (1:1000; Cell Signaling), mouse anti-p300 (1:1000; ab14984), rabbit anti-PCNA (1:1000; ab18197), mouse anti-α-tubulin clone B512 (1:5000; Sigma), rabbit anti-PAR (1:1000; Trevigen), rabbit anti-PARP1 (1:1000; Cell Signaling). The following antibodies were used for immunofluorescence: mouse anti-AIM-1 (1:600; BD), rabbit anti-PCNA (1:700; ab18197), mouse anti-GFP (1:500; Roche). Secondary HRP-conjugated antibodies for western blotting (Jackson ImmunoResearch) or IRDye fluorescent dye-conjugated antibodies (LI-COR) were used at 1:10000 dilution. Secondary Alexa Fluor® antibodies for immunofluorescence (Life Technologies) were used at 1:500 dilution.

Cell lysis

Cells were harvested by scraping with cold PBS and lysed in lysis buffer containing 50 mM Tris–Cl pH8, 150 mM NaCl, 1% Triton, 1 mM DTT, 50 U/ml benzonase (Novagen), pro-

tease inhibitors (Complete Mini Protease Inhibitor Cocktail Tablets, EDTA-free; Roche) for 1 h with rotation at 4°C.

FLAG co-immunoprecipitation

Anti-FLAG M2 magnetic beads (Sigma) were equilibrated by washing the beads twice with TBS. Lysates were incubated with the beads for 2 h at 4°C with rotation. Beads were washed three times with the lysis buffer and eluted with 3xFLAG peptide (Sigma).

Silver staining

Gels were washed three times with deionized water, fixed for 1 h in 30% ethanol and 5% acetic acid, washed four times with deionized water and incubated briefly with 0.02% sodium thiosulfate. After rinsing in deionized water, gels were incubated for 45 min in 0.2% $AgNO_3$ wrapped in aluminium foil, rinsed and developed in 2.4% Na_2CO_3, 0.04% formaldehyde and 0.0012% sodium thiosulfate. The reaction was quenched with 2% acetic acid and 4% Tris base.

Gel digestion

Excised gel bands were cut in half and digested separately with trypsin and chymotrypsin. Gel pieces were washed four times alternately in 100 mM ammonium bicarbonate (ABC) buffer and 50% ABC–50% acetonitrile buffer. The samples were reduced with 1 mg/ml DTT in ABC buffer for 30 min at 57°C and alkylated with 28 mM methyl methanethiosulfonate in ABC buffer for 30 min in the dark. Gel slices were washed four times as before and dried in a vacuum-concentrator. The gel slices were digested with 12 ng/μl of trypsin in the ABC buffer overnight at 37°C or 12 ng/μl of chymotrypsin in the ABC buffer at 25°C for 5 h. The supernatants were transferred and stored a 4°C and the gel slices extracted with 5% formic acid and 10 min sonication in a cooled ultrasonic bath three times. The supernatants were combined and analysed by mass spectrometry for both enzymes separately.

Mass spectrometry

Digested peptides were analysed on an UltiMate 3000 HPLC RSLC nano system (Thermo Scientific) coupled to a Q Exactive or Q Exactive Plus mass spectrometer (Thermo Scientific), equipped with a Proxeon nanospray source (Thermo Scientific). Peptides were loaded onto a trap column (PepMap C18, 5 mm × 300 μm ID, 5 μm particles, 100 Å pore size; Thermo Scientific) and separated on an analytical column at 30°C (PepMap C18, 500 mm × 75 μm ID, 3 μm, 100 Å; Thermo Scientific) with an elution gradient starting from 98% mobile phase A (water:formic acid, 99.9:0.1, v/v) and 2% B (water:acetonitrile:formic acid, 19.92:80:0.08, v/v/v), ramping to 35% B over 120 min followed by a 5-min gradient to 80% B. The mass spectrometer was operated in data-dependent mode, survey scans were obtained in a mass range of 380–1650 m/z, at a resolution of 70 000 at 200 m/z and an AGC target value of 3E6. The 12 most intense ions were selected for fragmentation with an isolation width of 2 m/z, fragmented in the HCD cell at 27% collision energy and the spectra recorded at a target value of 1E5 and a resolution of 17500. Peptides with a charge of +1 were excluded from fragmentation, the peptide match and exclude isotope features were enabled, and selected precursors were dynamically excluded from repeated sampling for 10 s.

Raw data were processed using Proteome Discoverer (version 2.1.0.81, Thermo Scientific) and the MS/MS spectra were searched using Mascot 2.2.07 (Matrix Science) against the human Swissprot protein sequence database. For a first search only the trypsin digested samples were searched and β-methylthiolation of cysteine was set as a fixed, oxidation of methionine and acetylation of lysine as variable modifications. The identified proteins were filtered at 1% PSM and protein FDR and a Mascot score of >30 and the resulting protein list was exported to a FASTA file for a second search on the trypsin and the chymotrypsin datasets using an extended set of variable modifications: phosphorylation (on S,T,Y), mono-, di- and trimethylation (on K), ubiquitinylation (on K, as GG or RGG), mono-ADP-ribosylation (on E,K,N,R,S), and sulfonation (S,T,Y). *O*-Sulfonation is a chemical modification occurring commonly on silver-stained proteins and might create artefacts in the identification of phosphopeptides. The higher mass deviation and the differential behavior in MS2 fragmentation concerning neutral losses can be used to differentiate these two modifications. However, as phosphorylation is not the main focus of this manuscript we chose not to further validate the corresponding sites. For Mascot search the peptide mass tolerance was set to ±5 ppm and the fragment mass tolerance to ±0.03 Da. Trypsin (set as specifically cleaving C-terminal to K or R but not if P follows) or chymotrypsin (set as specifically cleaving after F, L, W, Y but not if P follows) were specified as enzymes and two missed cleavages were allowed. The result was filtered at a 1% false-discovery rate (FDR) using the Percolator algorithm integrated in Proteome Discoverer (19) and at 1% protein FDR in the Proteome Discoverer consensus step. Additionally, peptides were required to have a minimum length of seven amino acids and the dataset was filtered at the PSM level at an ion score of ≥5 to obtain higher stringency for identifications. The localization of the sites of variable modifications within the peptides was performed with ptmRS, a node available for Proteome Discoverer, which is based on phosphoRS (20). For the PARG coverage map only sites with a probability of ≥75% were included, in all other data provided also sites with lower probabilities were retained. Proteome Discoverer analysis results were exported and converted to a summary report using custom tools. Spectra of all PSMs with evidence for the acetylation site K409 were annotated in the xiSPEC spectrum viewer (http://spectrumviewer.org) and are provided in Supplementary Figure S3.

Circular dichroism

Molar ellipticity values [θ] of 0.12 mg/ml of PARG 1–447aa in 10 mM K-Phosphate, pH 7.3 were recorded over a range of 260–185 nm wavelengths at room temperature using a Chirascan-plus (Applied Photophysics Ltd.) circular dichroism spectrometer.

Fluorescence lifetime imaging-fluorescence resonance energy transfer (FLIM-FRET)

U2OS cells seeded on 35 mm glass-bottom dishes were transfected with 500 ng of PARG–EGFP and 500 ng of mRFP-empty or mRFP–PCNA plasmids. FLIM-FRET measurements of co-transfected cells were performed 24 h after transfection using a time-domain fluorescence lifetime imaging setup (MicroTime 200, PicoQuant, Berlin) equipped with hybrid PMA detectors, a stable-Z environmental control and an objective heater system (Bioptechs). Excitation was achieved with a 485 nm pulsed laser diode (40 MHz repetition rate; pulse width ∼100 ps) and emission detected through a suitable interference bandpass filter (525/45 Semrock). The confocal pinhole was fixed at 30 μm. A 60 × 1.2 NA water immersion objective (UPlanSApo, Olympus) was laterally scanning the cells to generate 2D fluorescent lifetime maps with an effective pixel size of 0.1–0.22 μm. SymPhoTime 64 v2 software (PicoQuant, Berlin) was used for least-squares decay curve fitting over constrained regions of interest defined by the nucleus. Prior to analysis all data was re-convolved with the Instrument Response Function (IRF) measured at the probed excitation wavelength. The PARG-EGP lifetime in the absence of the acceptor-bound PCNA was best fit throughout the nucleus by a double exponential with τ_d ∼1.6 ns and τ_d ∼2.5 ns of comparable weighting (inset in top panel of Figure 2H). Amplitude weighted averages of the measured donor lifetimes were used to calculate the FRET efficiency (E), which is given by $E = (\tau_d - \tau_{da})/\tau_d$, where $<\tau_d>$ and $<\tau_{da}>$ are the amplitude averaged donor lifetimes in the absence and presence of acceptor fluorophores respectively.

X-ray crystallography

A 10-fold molar excess of the PARG peptide was incubated with 10 mg/ml of PCNA. Co-crystals were grown using the sitting-drop vapor diffusion technique. Crystallization conditions were optimized to 0.1 M Tris–HCl pH 7.5, 20% PEG 3350, 0.2 M ammonium acetate at 22°C. The data set has been collected at the beamline ID232 (ESRF, Grenoble) at 100 K using a wavelength of 0.968 Å. The data frames were processed using the XDS package (21), and converted to mtz format with the program AIMLESS (22). The structure was solved by using the molecular replacement program PHASER (23) using atomic coordinate of native human PCNA as a search model (pdb code: 1VYM). The structure was then refined with REFMAC (22,24) and Phenix Refine (25) and rebuilt using Coot (26). Data collection and refinement statistics are reported in Table 1.

Molecular dynamics (MD) simulations

The X-ray structure of the PARG–PCNA complex was protonated and repaired for the missing atoms using the PDB2PQR utility (27). The N- (402-QHGK) and C-terminal (A420) residues of the 402-QHGKKDSKITDHFMRLPKA-420 PARG peptide not visible in the X-ray structure were added manually to the X-ray conformation of the peptide. Further calculations were performed using GROMACS 4.5.1 package (28) and Amber99SB-ILDN force-field parameters (29). The system was placed into a 70 × 70 × 70 $Å^3$ rectangular box, energy minimized and solvated with TIP3P water molecules (30). Additional Na^+ ions were added to reach electroneutrality. The system was subsequently energy minimized and subjected to an MD equilibration over 30 000 steps using a 0.5-fs time step and 250000 steps using a 1-fs time step. Finally, 3 independent replicates were simulated for 200 ns using a 2-fs time step. A twin-range (10/14 Å) spherical cut-off function was used to truncate the van der Waals interactions. Electrostatic interactions were treated using the particle-mesh Ewald summation (real space cut-off 10 and 1.2-Å grid with fourth-order spline interpolation). MD simulations were carried out using 3D periodic boundary conditions in the isothermal−isobaric (NPT) ensemble with an isotropic pressure of 1.013 bar and a constant temperature of 310 K. The pressure and temperature were controlled using a Nose-Hoover thermostat (31) and a Parrinello-Rahman barostat (32) with 0.5 and 10 ps relaxation parameters, respectively, and a compressibility of 4.5 × 10^{-5} bar^{-1} for the barostat. Bond lengths were constrained using LINCS (33).

Analysis of MD trajectories

The cluster analysis for the concatenated independent replica trajectories was performed using the g_cluster utility from GROMACS package (with a 1.1-Å backbone RMSD cut-off for the neighbouring complex structures). The statistics of direct contacts between PCNA and modelled peptides was obtained using the g_dist utility from the GROMACS package (with a 3.5-Å cut-off distance between the centre of mass of every peptide sidechain and any atom of PCNA). The analysis of H-bonds was carried out using VMD (34). The hydrophobicity values were mapped onto PCNA surface using PLATINUM (35). 3D visualisation was done in PyMol (36).

Immunofluorescence

U2OS cells were seeded on coverslips, transfected with PARG-YFP plasmids and fixed after 24 h with 4% formaldehyde + 0.1% Triton in PBS for 10 min, washed twice in PBS for 5 min followed by a 5-min fixation with –20°C methanol. Cells were subsequently permeabilised with 0.5% Triton–PBS for 8 min, washed three times with PBS and blocked for 1 h with 1% BSA–0.1% Tween–PBS. Coverslips were incubated in appropriate dilutions of primary antibodies for 1 h at RT, washed three times with PBS and incubated in 1:500 dilutions of secondary antibodies for 1 h at RT. After two washes with PBS, coverslips were incubated for 5–10 min in 1:10 000 dilution of DAPI (Life Technologies) in PBS, washed twice with PBS and mounted onto a drop of ProLong Gold antifade reagent (Life Technologies) on glass slides. Images were acquired with LSM710

Table 1. X-ray data collection statistics

Source ESRF	ID232
Wavelength (Å)	0.968
Resolution (Å)	47.67–2.57 (2.64–2.57)
Space group	$P2_1$
Unit cell (Å, °)	77.60, 153.60, 85.51; β = 96.9
Molecules (a.u.)	6
Unique reflections	62473 (4080)
Completeness (%)	99.1 (88.2)
R_{merge} [b]	0.260 (3.575)
R_{meas} [c]	0.293 (4.056)
CC(1/2)	0.992 (0.155)
Multiplicity	4.8 (4.3)
I/sig(I)	5.6 (0.5)
B_{Wilson} (Å^2)	52.9
R_{work} [e]/R_{free} [f]	24.6/29.1
r.m.s.d. bonds (Å)	0.009
r.m.s.d. angles (°)	1.52

[a]Values in parentheses are for the highest resolution shell.

[b] $R_{merge} = \frac{\sum_{hkl}\sum_{i=1}^{N}|I_{i(hkl)}-\bar{I}_{(hkl)}|}{\sum_{hkl}\sum_{i=1}^{N}I_{i(hkl)}}$

[c] $R_{meas} = \frac{\sum_{hkl}\sqrt{N/(N-1)}\sum_{i=1}^{N}|I_{i(hkl)}-\bar{I}_{(hkl)}|}{\sum_{hkl}\sum_{i=1}^{N}I_{i(hkl)}}$

where $\bar{I}_{(hkl)}$ is the mean intensity of multiple $I_{i(hkl)}$ observations of the symmetry-related reflections, N is the redundancy.

[e] $R_{work} = \frac{\sum||F_{obs}|-|F_{calc}||}{\sum|F_{obs}|}$

[f]R_{free} is the cross-validation R_{factor} computed for the test set of reflections (5%) which are omitted in the refinement process.

confocal microscope (Zeiss), mounted on Zeiss Axio observer.Z1 equipped with Plan-Apochromat 63×/1.4 oil immersion lenses, a 405 nm laser diode (1.7 μW laser power at the sample), a 488 nm Argon laser (2.8 μW), a 561 nm DPSS laser (23.2 μW) and a 633 nm HeNe laser (1.7 μW). Images were acquired with Zen software (version 2.1, Zeiss) and processed with ImageJ.

3D-structured illumination microscopy (3D-SIM)

U2OS cells seeded on high precision borosilicate coverslips (0.170 ± 0.005 mm; LH22.1 Roth Labware) were transfected with 500 ng PARG–EGFP plasmids. The coverslips were fixed, blocked and stained with rabbit anti-PCNA antibody and mouse anti-GFP antibody followed by anti-rabbit Alexa Fluor® 568 and anti-mouse Alexa Fluor® 488 according to standard immunofluorescence procedure (see above). Vectashield H1000 was used for mounting the coverslips onto slides. 3D-SIM images were taken on a GE OMX v4 Blaze 3D Structured Illumination Microscope (3D-SIM) using 488 and 561 nm excitation lasers. The images were reconstructed with the SoftworX (GE Healthcare) software package, using Optical Transfer Functions (OTFs) calculated from the measured Point Spread Functions (PSFs) of 100 nm beads for each of the spectral channels. Lateral (chromatic) image registration for the two spectral channels was performed by imaging the scattered signal from a finely patterned metal slide following the standard protocol provided by the instrument manufacturer. Colocalization of foci was quantified by calculating the Pearson's colocalization coefficient (R_{coloc}) in both acquired channels using the Colocalization Threshold macro in Fiji (ImageJ 2.0.0 1.49v). Thresholded images were processed with the image calculator in ImageJ to only display pixels that were identical in both channels. Volume Viewer in ImageJ was used to generate overlay images.

Isothermal titration calorimetry (ITC)

All ITC experiments were carried out at 25°C on an iTC200 Microcalorimeter (GE Healthcare) with a 200 μl cell capacity and 40 μl syringe volume. A degassed 50 mM NaCl, 25 mM Tris–Cl pH 7.4 buffer was used for all solutions and for the control measurements. Twenty injections (starting with a 0.4 μl pre-injection followed by 19 injections of 2 μl) with a spacing of 150 s and stirring speed of 800 rpm were carried out. Concentrations ranged from 1.5–2 mM for the peptides and 150–200 μM for the purified PCNA constructs. All measurements were carried out at $T = 298.15$ K; the control injections were subtracted from sample measurements to correct for the heat during dilution. The data points were analyzed with the MicroCal Origin 7.0 software using a one-site binding model. The total heat exchanged with PCNA during each injection of PARG peptides was fitted to a single site binding model and the fitted curve was used to extract the thermodynamic properties. The summary of thermodynamic data is provided in Supplementary Table S3.

FACS analysis

Cell cycle profiling was performed using propidium iodide staining. 10^6 cells were trypsinized, resuspended in full

medium, centrifuged at 1000 rpm for 5 min, washed once with PBS and centrifuged again. The pellet was resuspended in 0.8 ml PBS and 2.2 ml ice-cold methanol while vortexing slowly. Cells were fixed at –20°C overnight. The following day, fixed cells were washed once with ice-cold PBS and resuspended in a propidium iodide buffer [(50 μg/ml propidium iodide (Sigma), 10 mM Tris–Cl pH 7.5, 5 mM $MgCl_2$, 200 μg/ml RNase A (Sigma)] and analysed using Zytofluorometer FACSCalibur and FlowJo version 7.5.5.

Laser microirradiation spinning disc microscopy

U2OS cells seeded on 35 mm glass-bottom dishes (175 ± 15 μm; Greiner Bio-One) were transfected with 1 μg PARG-YFP plasmids 24 h prior to imaging and presensitized with 10 μM 5-bromo-2′-deoxyuridine (BrdU; Sigma) 16 h prior to imaging. Laser microirradiation was performed on a spinning disc confocal microscope (Visitron) equipped with a 355 nm pulsed laser (iLASpulse; Roper), a high-speed/high-resolution camera (Evolve™ EMCCD; Photometrics), and an environmental chamber to maintain the physiological conditions (37°C, 5% CO_2). The samples were visualized with Visitron spinning disc (Yokogawa CSU-X1) setup on a Zeiss AxioObserver Z1-stand using an EC Plan-NeoFluor 100x/1.30NA Oil Iris objective lens, excited with a 488 nm 100 mW diode laser; equipment control and image capture was handled by Visiview software (version 2.1.4; Visitron). Laser settings were: 0.08 μJ/pulse (200 W peak power × 400 ps pulse width), 20 kHz repetition rate, 2 ms pulse duration, 165 nm diffraction limited spot. Laser microirradiation across a nucleus was applied at 6 ms/pixel. Images were captured with an exposure time of 100 ms in 1 s intervals for 20 min. Maximum YFP intensities inside and outside the damaged area were measured using Fiji (2.0.0-rc-34/1.50a); the relative fluorescent intensity in the damaged area was calculated as a ratio (I_t/I_0) of intensity at a given time and the initial intensity (before the laser damage) and corrected for photobleaching using the whole nucleoplasm intensity.

Laser microirradiation split-view widefield microscopy

U2OS cells were transfected with 0.1 μg mRFP–PCNA and 0.9 μg PARG–EGFP and presensitized with BrdU as above. Acquisition was performed using a Zeiss Axio Observer inverse widefield microscope equipped with an environmental chamber and EC Plan-NeoFluor 100×/1.30NA objective. Excitation was carried out by a solid-state Spectra-X light engine (GFP and RFP excitation LEDs respectively filtered by a dual-band 468/553 filter and a single-band 554/23 filter). The pulse duration of the 355 nm laser was 5 ms/pixel along a line of 11 μm. Dichroic ZT405/488/561/640rpc (Chroma) was used. Emission path was split using the OptosplitII setup (Cairn research): Splitting Cube composed of the Chroma 512/42m, T570lpxr and Chroma ET570lp with additional filters for the green and red light path: LP515 and BP/605/70. Camera: sCMOS, pco.edge 4.2. Control and acquisition software Visiview: v3.1.0.5 and acquisition sequence: 60 time points with 20 s interval. Red and green channel were acquired in parallel with 100 ms exposition over 4–7 zsteps (1 μm interval). Fiji was used for image analysis. The image sequence was first z projected (maximum intensity); the maximum intensity of the recruitment was measured after Gaussian filtering. Using Matlab, the individual recruitments were corrected for photobleaching using the whole nucleoplasm intensity and recruitment was normalized by intensity at t_0 to study the recruitment amplitudes. In order to study the mechanism of the recruitment kinetics, the recruitment was then rescaled between 0 (max intensity at t_0) and 1 (max intensity).

Statistics

Error bars represent standard deviation or standard error of the mean (sem) for image analysis in Figure 10. Statistical significance was calculated using two-tailed Student's *t*-test. *P*-values smaller than 5% were considered statistically significant and indicated with an asterisk (*$P < 0.05$; **$P < 0.01$; ***$P < 0.005$).

RESULTS

PARG is acetylated at multiple sites

To identify PARG acetylation sites, human N3xFLAG-tagged PARG cDNA was transiently transfected into HEK293T cells, PARG was immunoprecipitated with anti-FLAG beads and subjected to mass spectrometry analysis. We identified 24 different acetylation sites in five independent experiments, most of which occur in the PARG regulatory region (aa1–460) (Figure 1A and Supplementary Table S1). PARG acetylation was confirmed by western blotting with an anti-acetyl-lysine (anti-AcK) antibody, but only under conditions of overexpression of various lysine acetyltransferases (KATs) and treatment with the HDAC deacetylase inhibitor trichostatin A (TSA) (Figure 1B).

PARG interacts with PCNA via a non-canonical PIP-box

Mass spectrometry analysis of the PARG interactome in HEK293T cells confirmed the already reported PARG–PCNA interaction (Supplementary Figure S1, Supplementary Table S2 and Supporting Information). Alanine mutation of 19 out of 24 acetylation sites revealed that only K409A mutation led to a complete loss of interaction between PARG and PCNA by co-immunoprecipitation (Supplementary Figure S2). Mass spectrometry analysis of PARG yielded 10 spectra with convincing evidence for acetylation of K409 (Supplementary Figure S3). Methylation, ubiquitination or mono-ADP(ribosyl)ation were not identified on K409. To test whether K409 acetylation mediated PCNA binding, we generated acetylation-mimicking K409Q mutant, which also showed no PCNA binding (Figure 2A-B). Close inspection of the K409 region revealed that it is part of a non-canonical PIP-box (D407-F414) also found in translesion synthesis polymerases Pol η, κ and ι (37) (Figure 2C). Unlike canonical PIP-boxes, non-canonical PIP-boxes do not have glutamine (Q) as the first residue and follow the pattern x-x-x-**h**-x-x-**a-a** (38). While TLS polymerases harbour acidic amino acids (DE) at position 5 following a hydrophobic residue, PARG non-canonical PIP-box has a TD motif found in some canonical PIP-boxes with high binding affinity for PCNA, such

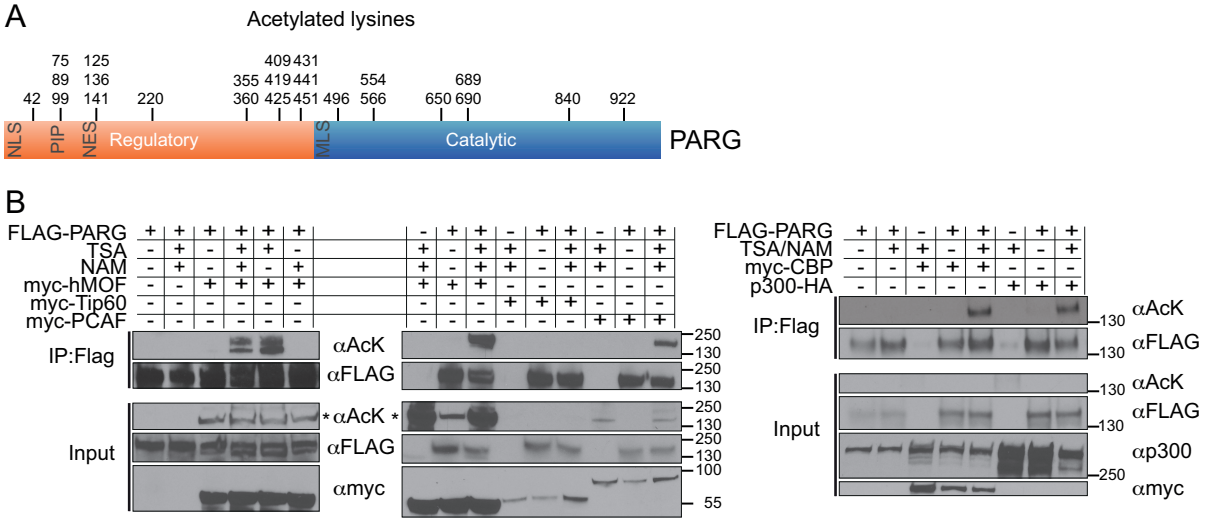

Figure 1. PARG is acetylated at multiple sites *in vivo*. (**A**) Schematic presentation of lysine residues in the PARG regulatory and catalytic region that were found acetylated by mass spectrometry analysis. (**B**) FLAG co-immunoprecipitation of transiently co-transfected FLAG-PARG and myc-hMOF, myc-Tip60, myc-PCAF, myc-CBP and p300-HA acetyltransferases. 10 μM TSA and 20 mM NAM were added 6 h prior to cell lysis. Asterisk denotes a non-PARG band migrating at the same height in inputs blotted with anti-AcK.

as the CDK inhibitor p21 (39) and the replication licensing factor Cdt1 (40) (Figures 2C and 4A). The non-canonical PIP-box is located within the intrinsically disordered N-terminal regulatory region of PARG (Figure 2D and E). To test whether lysine positive charge is prerequisite for PCNA interaction, we generated the K409R mutation, which modestly rescued the PARG–PCNA interaction to one third of the wild-type level (28±14%; Figure 2A-B). This suggests that the K409 positive charge is only partially important for PARG–PCNA interaction.

We performed single-cell *in vivo* analysis of PARG–PCNA binding by fluorescence resonance energy transfer (FRET) in order to confirm direct PARG–PCNA interaction (Figure 2F–K, Supporting Information and Supplementary Figure S4). FRET measurements can be used to confirm the nanoscale proximity of two fluorescent species through near-field electronic energy transfer from 'donor' to 'acceptor' fluorophores as illustrated in Figure 2F. We used time-resolved fluorescence lifetime imaging (FLIM) to investigate the FRET efficiency between PARG–EGFP (donor) and mRFP–PCNA (acceptor) in nuclei of live G1/G2 and S-phase U2OS cells (Figure 2G-K and Supplementary Figure S4C–G). The amplitude-averaged lifetime for PARG–EGFP was $\tau_d = 2.0$ ns (Figure 2I). The presence of mRFP–PCNA was found to reduce the amplitude-averaged lifetime of EGFP to 1.60 ± 0.10 ns (Figure 2G–I), suggesting a minimum FRET efficiency of 21% in G1/G2 cells (Figure 2J). We can interpret the 21% FRET efficiency as a clear sign of the physical proximity of PARG and PCNA, bearing in mind that the EGFP-mCherry fusion via a short amino-acid linker yields a FRET efficiency of ∼25% (41). A significant decrease in PARG–EGFP lifetime in the presence of mRFP–PCNA was also observed in S-phase cells (Supplementary Figure S4F). The lifetime of the K409A mutant did not, however, decrease in the presence of mRFP–PCNA, suggesting no interaction. In contrast, the K409R mutant exhibited a 0.23 ns reduction in the donor lifetime and a 1.7-fold reduction in the FRET efficiency relative to the wild-type PARG (Figure 2G–J). The loss of PARG–PCNA FRET due to the K409A mutation and a 58% rescue with the K409R mutation provide further evidence that the K409 residue is crucial for direct interaction between PARG and PCNA, with the lysine positive charge facilitating the interaction. PARP1/2 inhibition by olaparib did not affect the reduction in PARG–EGFP lifetime in the presence of mRFP–PCNA, indicating that PARG–PCNA interaction is not influenced by PAR (Figure 2K).

The thermodynamic parameters of PARG–PCNA interaction were measured *in vitro* by ITC. We were unable to purify the full-length PARG; thus, we measured binding between the full-length His_6-tagged PCNA and 19 aa-long PARG peptides (402-QHGKKDSKITDHFMRLPKA-420) spanning the K409 non-canonical PIP-box (Figure 3A and B). PCNA showed micromolar affinity towards the PARG peptide ($K_d = 3.3 \pm 0.4$ μM) with a stoichiometry of 1:1. K409A and K409R mutations decreased binding affinity towards PCNA 7.5- and 2-fold, respectively (Figure 3A and B). This is in agreement with the co-immunoprecipitation assay and the FLIM-FRET analysis, although the K409A mutation showed a stronger effect *in vivo* (in the context of a full-length protein) than *in vitro* (a short peptide) (discussed in more detail below). The K409-acetylated PARG peptide also yielded a 2-fold lower affinity towards PCNA (Figure 3A and B), which indicates that the K409 acetylation weakens PARG binding to PCNA. The putative N-terminal PIP-box (Q76-W82) did not bind PCNA *in vitro* (Supplementary Figure S5A), corroborating the previously shown lack of effect of the Q76A mutation on PCNA binding by co-immunoprecipitation (13). Interestingly, a shorter PARG non-canonical PIP-box peptide lacking four amino acids C-terminal to the consensus PIP-box motif (417-LPKA-420) showed a 14-fold lower affinity towards PCNA ($K_d = 45.3 \pm 5.7$ μM) (Supplementary Figure S5B and C). A similar phenomenon of binding

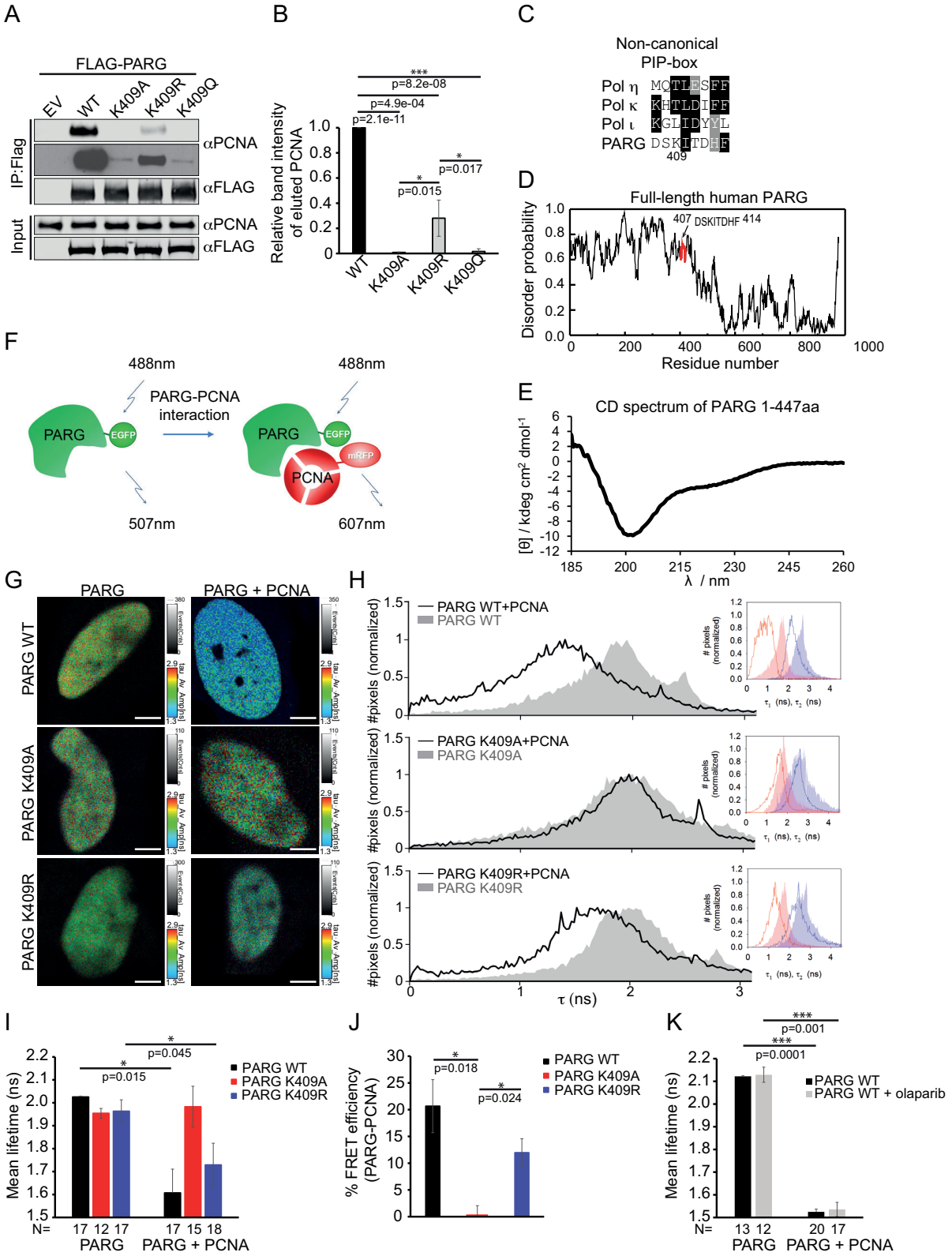

Figure 2. A non-canonical PIP-box mediates PARG interaction with PCNA *in vivo*. (**A**) K409 mutation abrogates PARG interaction with PCNA. Co-immunoprecipitation analysis of interaction between PCNA and FLAG-PARG K409A, K409R and K409Q mutants. 5% of input and 50% of eluate was loaded on the gels. (**B**) Fluorescent band intensity of K409 mutants relative to the wild-type PARG was quantified by normalizing eluted PCNA band intensity to the corresponding eluted FLAG-PARG band intensity from three independent experiments. (**C**) Alignment of non-canonical PIP-box motifs. (**D**) PARG non-canonical PIP-box motif is located within the disordered N-terminal PARG region. Disorder probability was calculated using IUpred software. (**E**) The circular dichroism (CD) spectrum of the N-terminal PARG region shows a negative minimum around 200 nm and a negative shoulder

stabilization via additional residues downstream from the PIP-box was also shown for the canonical PIP-box in p21 (39) and the non-canonical PIP-box in the TLS polymerase Pol η (38).

To verify the relative contribution of the putative N-terminal PIP-box (Q76-W82) and the non-canonical K409 PIP-box to PARG interaction with PCNA, we generated multiple truncations and mutations of PARG and performed co-immunoprecipitation experiments (Figure 4). As previously reported, the PARG regulatory domain (1–469aa) is sufficient for PCNA interaction (13). The catalytic domain, however, was essential for PARG interaction with monoubiquitinated PCNA (Figure 4B; upper PCNA band). There was no difference in the interaction strength between 1–75aa (without the putative PIP-box) and 1–87aa (with the putative PIP-box) PARG truncations (Figure 4B). Furthermore, the Q76A mutation in the putative PARG PIP-box had no effect on the interaction and the interaction with PCNA was reduced–but not abolished–when the N-terminal segment (1–87aa) was removed (Figure 4B-C). The N-terminal segment also contains nuclear localization signal (NLS), which is essential for the nuclear localization of PARG where interaction with PCNA takes place (Supplementary Figure S6). Thus, we conclude that PARG–PCNA interaction is primarily mediated by the K409 non-canonical PIP-box and facilitated by PARG nuclear localization.

Hydrophobic and electrostatic interactions mediate the binding of the PARG non-canonical PIP-box to PCNA

Our *in vitro* and *in vivo* experiments revealed that the K409R mutant, which preserves the positive charge, can only partially rescue PARG–PCNA interactions. To understand this interaction at the molecular level, we solved the crystal structure of PCNA in complex with the PARG non-canonical PIP-box peptide (402-QHGKKDSKITDHFMRLPKA-420) at 2.57 Å resolution (Figure 5). PCNA is a functional trimer forming a doughnut-like quaternary assembly (Figure 5A). Two PCNA trimers, with all six subunits bound to PARG peptides, were found in the asymmetric unit. The conformation and position of bound peptide are the same for all the complexes in asymmetric unit (Figure 5B). Small differences were observed in the length of modeled peptides according to their visibility in electron density map and vary from 14 (K406–K419) to 10 residues (K406–M415).

Location of the PARG non-canonical PIP-box peptide on PCNA corresponds to that of other non-canonical as well as canonical PIP-box peptides. The PARG peptide is nested in the hydrophobic region of PCNA skirted by negative electrostatic potential (Figures 5C, and 8A). Each PARG peptide extends along the binding interface of PCNA and forms a characteristic single 3_{10}-helical turn between residues I410 and H413 (Figure 5D). This single helical turn protrudes into the hydrophobic pocket of PCNA in the central loop region between M40 and L47 (Figure 5D). Hydrophobic residues I410 and F414 protrude into the hydrophobic pocket of PCNA formed by the C-terminal portion of the interdomain connector loop (IDCL; M119 - Y133) and the body of the protein (Figure 5D). I410 is completely buried in the pocket lined with hydrophobic side chains M40 and L47 and Cβ of Y250, while F414 aromatic side chain is sandwiched between I128 and P234, and stabilized by aromatic stacking interaction with Y250 (Figure 5C and D). Aromatic-proline interactions (CH/π interactions) (42) occur between H413 and P234, further stabilizing PARG–PCNA interaction (Figure 5D). The TD motif (T411–D412) was previously shown to be critical for p21 and Cdt1 canonical PIP-box binding to PCNA (39,40), while aromatic residues (Y or F) in the C-terminal part (position 7 and 8) serve a stabilizing function (43,44). Although PARG PIP-box contains histidine H413 at position 7, this residue is engaged in stabilizing interactions similar to aromatic residues at the equivalent position in other PIP-boxes. Indeed, ITC experiments with the 402-QHGKKDSKITDHFMRLPKA-420 peptides bearing different mutations confirmed that H413, T411 and F414 are essential for PARG binding to PCNA (Figure 5F).

The aforementioned residues engage in hydrophobic interactions with PCNA. PARG K409, however, binds PCNA via a mixed hydrophobic and electrostatic mode (Figure 5E). The ϵ-amino group of K409 forms a hydrogen bond with the main-chain carbonyl group of S43, while its aliphatic side chain forms hydrophobic interactions with PCNA H44 and V45 (Figure 5E). The position of K409 within the pocket is additionally stabilized by the hydrogen bond between amide nitrogen of the neighboring residue PARG I410 and carbonyl oxygen of PCNA H44 (Figure 5E). The hydrophobic contribution of the lysine side chain was confirmed by the K409L mutation, which showed a neutral effect on PCNA binding (Figure 5F).

Residues K406-S408 of the PARG peptide interact with the very C-terminus of PCNA through the main chain-main chain hydrogen bonding between carbonyl oxygen of K406 and amide nitrogen of S408 of PARG, and the amide nitrogen of I255 and carbonyl oxygen of P253 of PCNA, respectively (Figure 5D). A single salt bridge exists between R416 of PARG and E124 of PCNA (Figure 5D), which seems to be of transient nature, as the density for side chains of R416 and E124 is missing in some of the molecules. ITC analysis

←

around 222 nm, suggesting high intrinsic disorder with a minor fraction of α-helix. (**F**) Schematic presentation of FRET resulting from the PARG–EGFP and mRFP–PCNA interaction. (**G**) Amplitude-averaged fluorescence lifetime map of PARG–EGFP in the nucleus of G1/G2 U2OS cells expressing PARG–EGFP + mRFP-empty (left) and PARG–EGFP + mRFP–PCNA (right). The reduced lifetime in the latter (blue) compared to the former (green) is the result of FRET between EGFP and mRFP. (**H**) Distribution of amplitude-averaged lifetime in PARG WT, K409A and K409R-expressing cells (solid black line). The distributions for the corresponding empty (no acceptor) cells are shown in shaded grey. [Insets: distribution of the two individual fitted lifetime components for PARG–EGFP + mRFP–PCNA cells (solid lines) and PARG–EGFP + mRFP-empty (shaded).] (**I**) Mean values of the amplitude averaged lifetime for U2OS cells expressing PARG–EGFP and mRFP-empty or PARG–EGFP and mRFP–PCNA. (**J**) Calculated FRET efficiency for wild-type, K409A and K409R PARG–EGFP in the presence of mRFP–PCNA. (**K**) Mean values of the amplitude averaged lifetime for U2OS cells expressing PARG–EGFP and mRFP-empty or PARG–EGFP and mRFP–PCNA in the presence of 10 μM olaparib for 1–2 h.

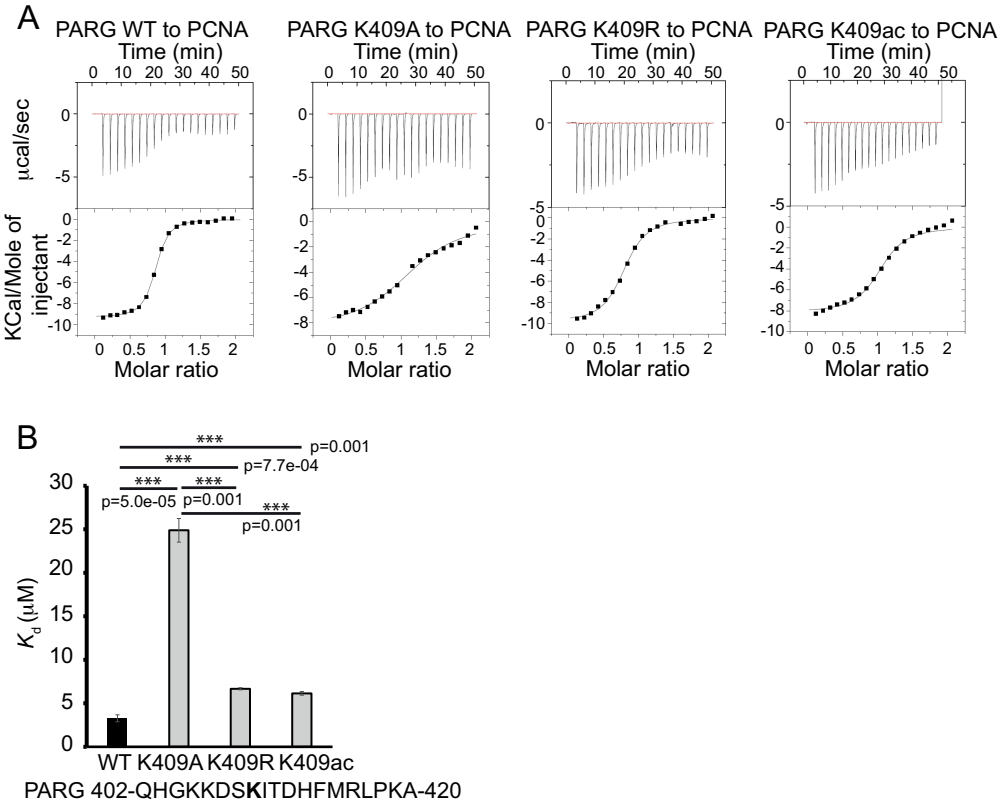

Figure 3. A non-canonical PIP-box mediates PARG interaction with PCNA *in vitro*. (**A**) ITC analysis of binding affinity between full-length his_6-tagged PCNA (150 µM) and PARG wild-type, K409A, K409R and K409ac peptides (1.5 mM). (**B**) Dissociation constants (K_d) for wild-type, K409A, K409R and K409ac peptides. Peptide sequence is indicated under the graph; K409 is indicated in bold. Average from two independent experiments with two technical replicates are shown. Error bars represent sd.

showed negligible effect of the R416A mutation on PCNA binding (Figure 5F).

Interestingly, the binding mode of the PARG non-canonical PIP-box is more similar to the canonical PIP-boxes (Figure 6A and B). Structural comparison of the PARG non-canonical PIP-box with other non-canonical peptides from Pol κ and Pol η (38) (Figure 6A) gave RMSDs of 0.58 to 2.04 Å for equivalent Cα atoms, with the largest differences in conformation and position of the main- as well as side-chain being in the first three amino acids (409-DSK) of the bound peptide. Superposition with canonical PIP-box peptides from p21 (45), polymerase delta p66 subunit and FEN1 (39) (Figure 6B) yielded RMSD values between 0.34 and 0.42 Å, suggesting that the PARG PIP-box is a new type of non-canonical PIP-box with a canonical mode of PCNA binding. PARG D407 is replaced with the common Q in canonical PIP-boxes, while K409 is replaced with S/R in canonical PIP-boxes or L/T in non-canonical PIP-boxes (Figures 4A and 6). In canonical PIP-boxes the side chain of the Q residue within the signature motif is stabilized via hydrogen bonds to the main-chain of A252, V45 and to solvent molecules; in the PARG peptide D407 exerts its stabilising function by electrostatic interaction with K254 and by somewhat weaker hydrogen bonding to the A252 main-chain. However, D407A mutant did not show any effect on PCNA binding according to ITC (Figure 5F).

In order to probe the importance of non-canonical PIP-box residues *in vivo*, we performed co-immunoprecipitation of full-length FLAG-tagged PARG wild-type and mutants in HEK293 cells (Figure 7). *In vivo* co-IP data showed good agreement with *in vitro* ITC data for D407, K409, T411, H413 and M415 (Figures 5F and 7). However, D412A resulted in a complete loss of *in vivo* binding, whereas *in vitro* binding was reduced by only 2.6-fold. Similarly, R416A led to an almost complete loss of *in vivo* binding with little effect *in vitro*. Conversely, F414A caused a 12.5-fold reduction *in vitro*, but had no effect *in vivo*. However, F414D mutation completely abrogated PCNA binding *in vivo* (Figure 7C and D). We expanded the *in vivo* analysis to additional mutations, which confirmed that the hydrophobic residue in the middle of the PIP-box, I410, is crucial for PCNA binding (Figure 7C and D). Interestingly, replacement of D407 with canonical Q and H413 with canonical Y or F increased PARG–PCNA binding (Figure 7C and D), suggesting that sequence variations among PIP-boxes modulate PCNA binding affinity.

Dynamic binding of the PARG non-canonical PIP-box to PCNA

Given that the PARG non-canonical PIP-box is located in a highly disordered region of the full-length PARG (Figure 2D), its binding mode to PCNA may exhibit a high

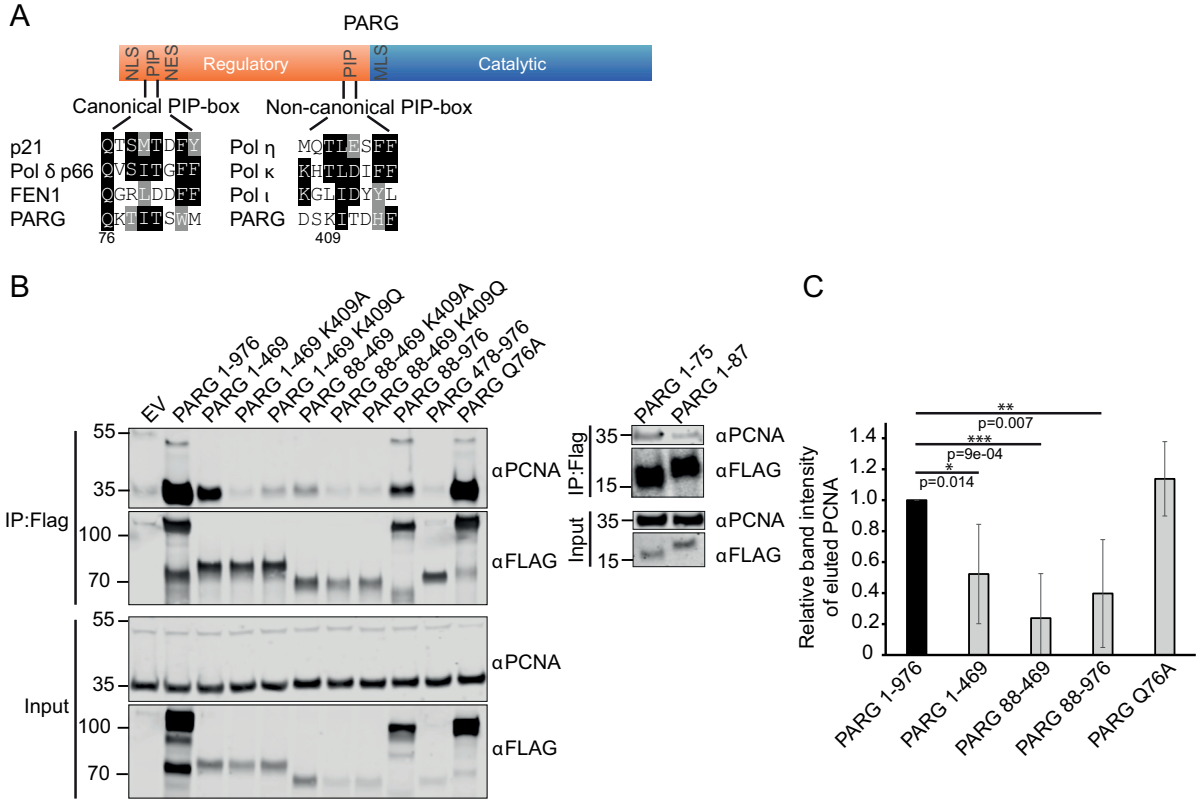

Figure 4. The putative N-terminal PIP-box is dispensable for PARG–PCNA interaction. (**A**) Location and alignment of PARG putative and non-canonical PIP-box. (**B**) Co-immunoprecipitation analysis of interaction between PCNA and FLAG-PARG truncation mutants and the putative PIP-box mutant Q76A. 5% of input and 50% of eluate was loaded on the gels. (**C**) Fluorescent band intensity of truncation mutants relative to the wild-type PARG was quantified by normalizing eluted PCNA band intensity to the corresponding eluted FLAG-PARG band intensity from three independent experiments. Error bars represent sd.

level of plasticity, as has been shown for a number of intrinsically disordered regulator proteins (46,47). Therefore, we used molecular dynamics (MD) simulations to characterize the dynamic binding mode of the PARG PIP-box, where the contribution of every residue to binding is captured with its statistical weights. We used the X-ray derived complex structure (Figure 5) as a starting conformation for the simulations. The N- and C-terminal fragments of the 402-QHGKKDSKITDHFMRLPKA-420 PARG peptide, which were not visible in the X-ray structure, were added for completeness. We performed three independent 200 ns MD simulations of the PCNA-PARG complex in a water box. The average RMSD from the starting configuration among these three runs is approximately 2.5 Å (Supplementary Figure S7), indicating that the X-ray-like PCNA-PARG complex structure is sufficiently stable in the case of the complete PARG peptide sequence. In agreement with the X-ray experiment, the terminal peptide fragments do not display any preferential orientation with respect to PCNA (Figure 8A).

Upon binding, the PARG peptide adjusts electrostatic and hydrophobic properties on its surface in order to match those of the PCNA interaction interface, which is characterized by a negative electrostatic potential and a prominent hydrophobic patch (Figure 5C, 8A). Particularly, the 3_{10}-helical turn of the PARG peptide fits snuggly into the hydrophobic pocket of the PCNA surface (Figure 8A). The PARG residues S408, K409, H413, R416, and L417 display a high frequency of contacts with PCNA and relatively small deviations between different MD runs (Figure 8B). Importantly, K409 and H413 preserve in MD their dominant interaction partners, which were identified in X-ray structure (Figure 8C). Thus, these residues appear to be important for the interaction with PCNA that is in the agreement with both *in vitro* and *in vivo* mutagenesis (Figures 5F, and 6). At the same time, in contrast to the well-defined binding position in the X-ray structure, in MD simulations F414 displays rather dynamic interactions, which vary between different MD runs (Figure 8B). This can potentially explain the moderate *in vitro* and negligible *in vivo* effects of the F414A substitution (Figures 5F and 6). For T411 and, particularly, D412, no significant interactions with PCNA were also observed in MD simulations (Figure 8B). While T411 may optimize the PARG surface for the binding in the PCNA hydrophobic pocket, the effect of this mutation remains unclear. The D412 sidechain forms stable H-bonds with the K409 main-chain or less frequently with the K409 side-chain in cases where its orientation is orthogonal to the PCNA surface (Figure 8C inset; Figure 8A). Thus, D412 side-chain in MD simulations contributes to the stability of the 3_{10}-helical turn. At the same time, the differences between the effect of the D412A substitution *in vivo*

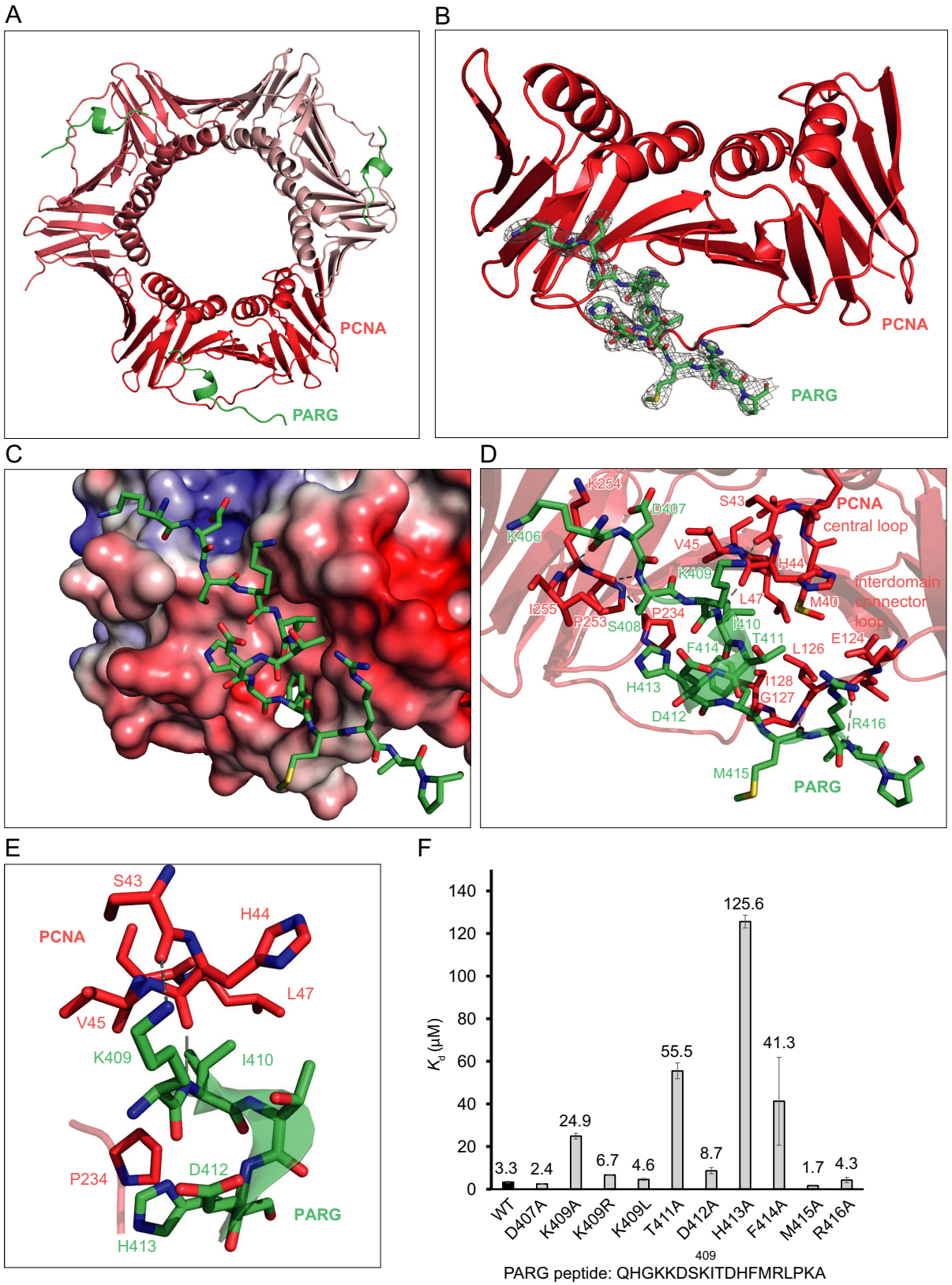

Figure 5. Co-crystal structure of the PARG non-canonical PIP-box peptide bound to PCNA. (**A**) Three PARG PIP-box peptides (green) are bound to a PCNA trimer (red). (**B**) PARG PIP-box peptide binds the interdomain connector loop (IDCL) of PCNA. (**C**) PARG PIP-box peptide is nested in the hydrophobic region of PCNA surrounded by negatively charged residues. The color coded electrostatic surface potential of PCNA was drawn using the Adaptive Poisson–Boltzmann Solver package within PyMol. The electrostatic potential ranges from −5 (red) to +5 (blue) kT/e. (**D**) Electrostatic and

and *in vitro* may suggest an additional interaction mode of the PARG non-canonical PIP-box with PCNA in the full-length protein background.

K409 mutation within the non-canonical PIP-box delocalizes PARG from S-phase replication foci

In order to evaluate the biological importance of the non-canonical PIP-box in mediating interaction with PCNA, we investigated whether K409 mutations affect PARG localization within PCNA replication foci. PARG was previously shown to form a punctate pattern in S-phase cells resembling replication foci and to co-localize with PCNA by confocal microscopy (13) (Figure 9A). In more than 80% of S-phase cells, PARG K409A mutant failed to form distinct S-phase foci but rather exhibited diffuse distribution akin to G1 or G2 cells (Figure 9A and B). A similar diffuse S-phase localization was reported for TLS polymerases with mutations in the PIP-box (44,48) or in the ubiquitin-binding domain required for binding monoubiquitinated PCNA (49). Foci formation was intact in 59% of S-phase cells expressing the K409R mutant, which is consistent with the observed partial rescue of PARG–PCNA interaction by mimicking the K409 positive charge (Figure 9A and B). Importantly, the K409L mutant exhibited wild-type properties (Figure 9A-B). PARG–PCNA colocalization was further investigated by super-resolution imaging on a commercial 3D-Structured Illumination Microscope (SIM). 3D-SIM analysis clearly showed that PARG co-localizes with PCNA in S-phase cells ($R = 0.43 \pm 0.14$; Figure 9C and D). On the other hand, K409A and K409R mutants displayed only 19% and 37% co-localization with PCNA relative to the wild type (Figure 9D).

Previous work has shown that the first 82 amino acids of human PARG are responsible for its nuclear localization and that the putative PIP-box mutant (Q76A) is defective in S-phase foci formation (8,13). The PARG 1–75aa truncation localizes in the nucleus; nevertheless, it is not able to form distinct S-phase replication foci, as it requires the putative PIP-box motif present in residues Q76-W82 (Supplementary Figure S6). The Q76A mutation was comparable to the K409R mutation regarding PCNA co-localization and S-phase foci formation (Figure 9). Q76A K409A double mutant did not exacerbate the phenotype of the K409A mutant, indicating that the non-canonical PIP-box is the primary PCNA interaction point (Figure 9B). Taken together, both the Q76 putative PIP-box and the K409 non-canonical PIP-box contribute to PARG localization in S-phase, although Q76 is dispensable for PARG–PCNA interaction. This may indicate that the putative PIP-box is required for interaction with another replication protein. Alternatively, the Q76 PIP-box may be in the 3D proximity of the K409 PIP-box and may thereby contribute to a more favorable interface for PCNA binding.

While the K409-mediated interaction with PCNA determined PARG localization within S-phase replication foci, the K409A mutation did not affect cell cycle progression, PARG nuclear localization, or its catalytic activity (Supplementary Figure S8).

K409 mutation compromises PARG recruitment to laser-induced DNA damage sites

PARG is known to be rapidly and strongly recruited to DNA damage sites induced by laser microirradiation in a PCNA- and PAR-dependent fashion (13). Imaging wild-type PARG-YFP recruitment in U2OS cells after damage with the 355 nm laser coupled to the spinning disc system reproducibly showed the maximum recruitment time of 80 s (Figure 10). K409A mutation diminished maximum PARG recruitment to about a half of the wild-type levels and increased the rate of dissociation (Figure 10A-B), indicating that K409 is important for both the rate and the magnitude of PARG recruitment to DNA damage sites. Q76A exhibited similar kinetics to K409A but higher amplitude, whereas K409R showed increased dissociation rate (Figure 10B). PARP1/2 inhibitors olaparib (AZD2281, Ku-0059436) (50) and talazoparib (BMN 673) (51) reduced the initial rate of recruitment of wild-type PARG and K409A (Figure 10C), confirming that PARG is recruited to laser-induced DNA damage sites in a PAR- and PCNA-dependent fashion (52). Weak PARG K409A recruitment in the presence of PARP1/2 inhibitors indicates the existence of a third recruitment pathway, as previously suggested (52). Taken together, our results show that PAR promotes the initial phase of PARG recruitment, while its interaction with PCNA determines PARG accumulation and stabilization at DNA damage sites.

K409 regulates PARG dissociation from DNA damage sites

The K409L mutant showed slower dissociation compared to the wild-type PARG (Figure 10B). The slower dissociation of the K409L mutant from laser-induced DNA damage sites may be due to the absence of acetylation that is necessary to destabilize PARG interaction with PCNA and promote PARG dissociation from damage sites. This would require PCNA to be retained at DNA damage sites during PARG dissociation. To test this, we performed split-view imaging with a single camera whereby PARG–EGFP and mRFP–PCNA were cotransfected in U2OS cells and their recruitment was followed simultaneously in the same cell (Figure 10D). While the initial phase of recruitment was very similar for PARG and PCNA, PCNA was found to dissociate slower than PARG and both PCNA and PARG exhibited slower dissociation kinetics when PARG K409L mutant was used (Figure 10D). This suggests that the stabilization of PARG–PCNA interaction via the K409L mutation modestly impairs PARG and PCNA dissociation from DNA damage sites and that modification of K409 by acetylation may regulate PARG and PCNA dissociation kinetics.

←

hydrophobic interactions between PARG PIP-box peptide and PCNA. (**E**) Electrostatic and hydrophobic interactions of PARG K409 with PCNA S43 and V45. (**F**) ITC analysis of the changes in binding affinities due to mutations of PARG PIP-box residues. Two independent experiments with two technical replicates were performed. Error bars represent sd.

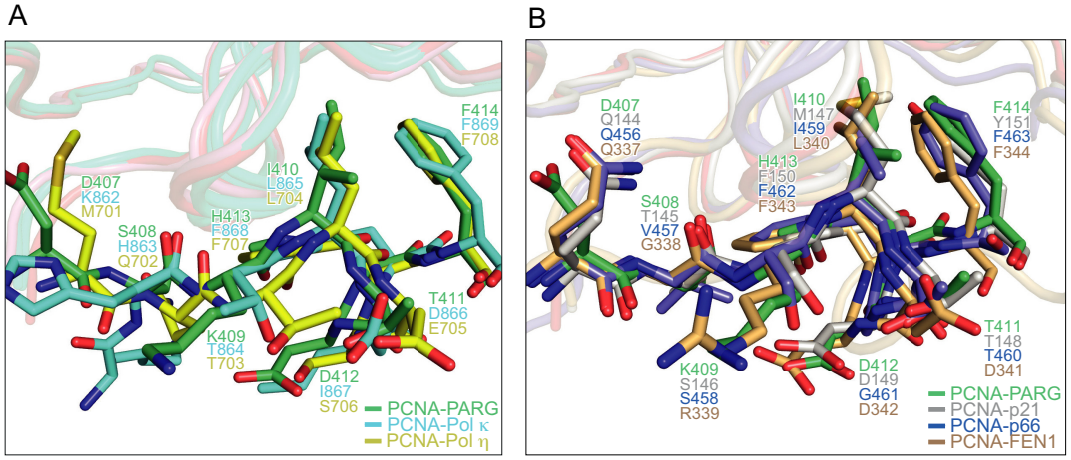

Figure 6. PARG non-canonical PIP-box binds PCNA in a canonical mode. (**A**) Overlay of crystal structures of the PARG non-canonical PIP-box peptide and non-canonical PIP-box peptides from Pol κ (2ZVL) and Pol η (2ZVK). (**B**) Overlay of crystal structures of the PARG non-canonical PIP-box peptide and canonical PIP-box peptides from p21 (1AXC), polymerase delta p66 subunit (1U76) and FEN1 (1U7B).

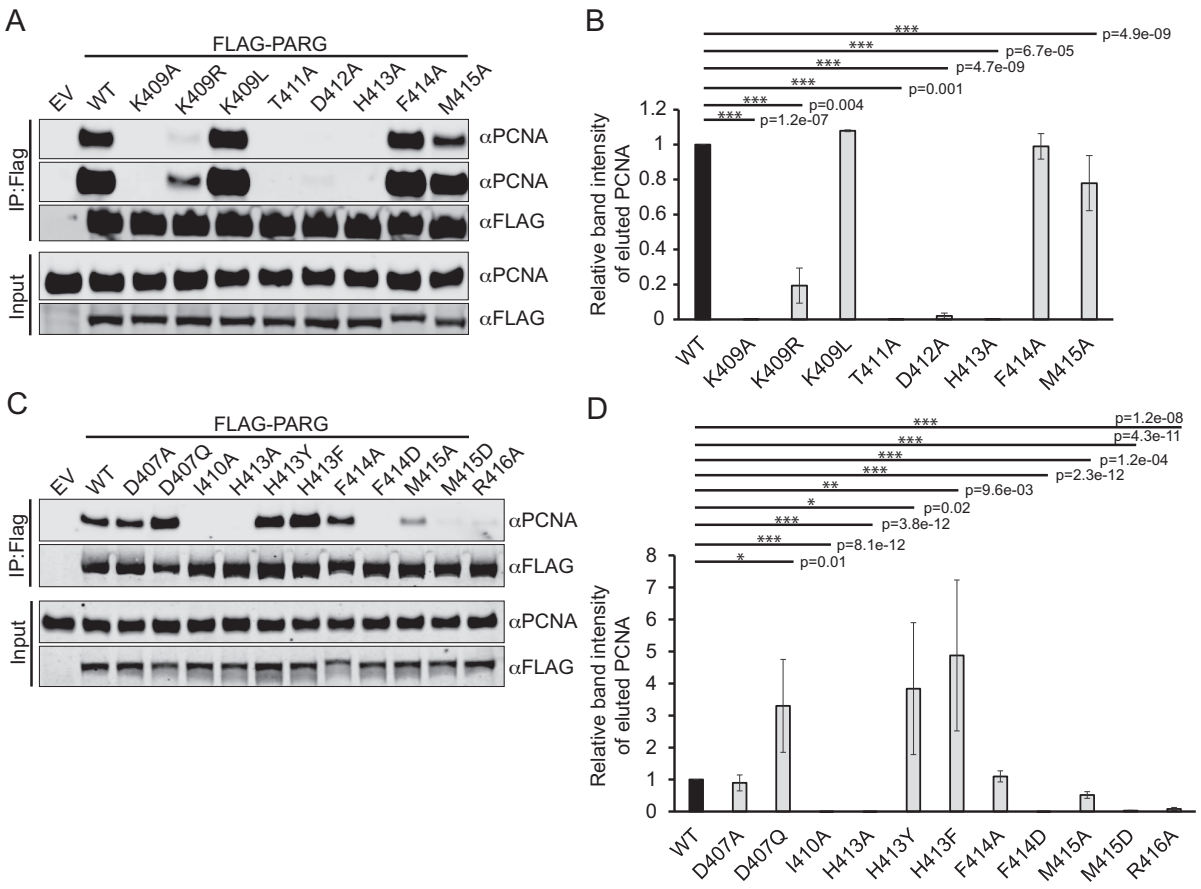

Figure 7. The effect of PARG mutations spanning the PARG non-canonical PIP-box on PCNA binding *in vivo*. (**A,C**) Co-immunoprecipitation analysis of interaction between PCNA and FLAG-PARG constructs. 5% of input and 50% of eluate was loaded on the gels. (**B,D**) Fluorescent band intensity of PARG constructs relative to the wild-type PARG was quantified by normalizing eluted PCNA band intensity to the corresponding eluted FLAG-PARG band intensity from three independent experiments. Error bars represent sd. P-values were calculated using Student's t-test.

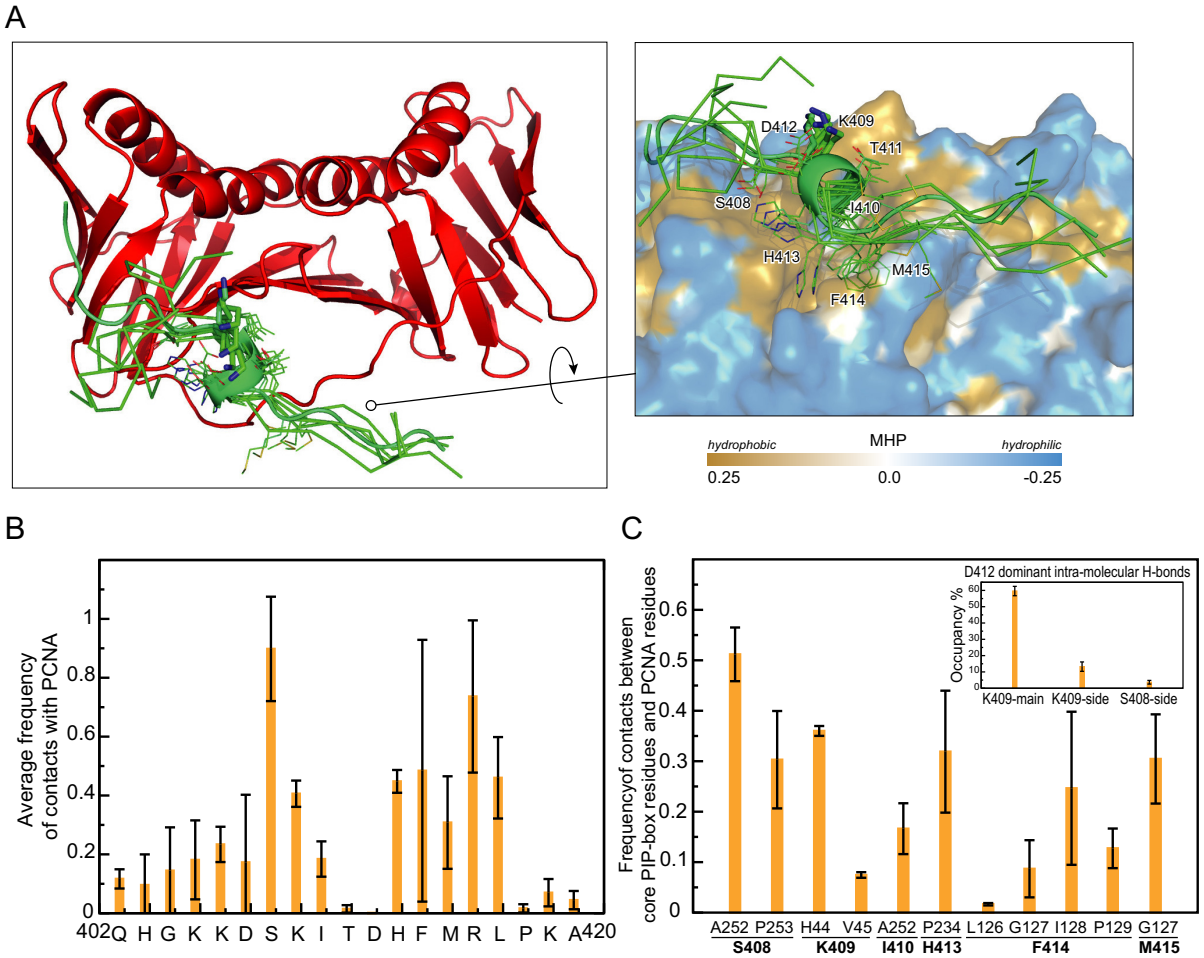

Figure 8. Dynamic interaction of the PARG peptide with PCNA. (**A**) Representative MD conformations of the PARG–PCNA complex obtained from the cluster analysis of concatenated MD trajectories (see Supplementary Figure S7 for details) and aligned in the reference frame of PCNA. PCNA is shown in cartoon (left panel) and surface representations (right panel), whereby the latter is coloured according to the molecular hydrophobicity potential (MHP). A PARG MD conformation closest to X-ray structure (backbone RMSD of 1.5 Å) is shown in cartoon representation. 'Core' interacting PARG residues are shown in line representation, while K409 is shown in stick representation. (**B**) Average frequency of contacts between PARG residues and PCNA, calculated from the MD simulations. (**C**) Detailed statistics for contact pairs of 'core' interacting PARG residues (bold characters). The inset shows intra-molecular H-bonds formed by D412.

DISCUSSION

Poly(ADP-ribosyl)ation regulates a variety of cellular processes by providing a rapid and transient modulation of protein-protein and protein-DNA interactions (1). PAR levels are tightly controlled by PARG, which has a high specific activity towards PAR (53). Recently, the PARG catalytic mechanism has been thoroughly investigated (7,10); however, the available information on the regulation of PARG interactions has remained scarce. The N-terminal PARG regulatory region is unstructured and hence highly amenable to post-translational modifications. Our mass spectrometry analysis revealed that of the 64 PARG lysines, 24 are acetylated under basal conditions. Lysine acetylation may regulate protein activity, cellular localization, protein-protein and protein-nucleic acid interactions by eliminating the positive charge from the lysine side chain or by steric hindrance (54). Although acetylation does not affect PARG activity or cellular localization, we found that one of the acetylation sites, K409, is essential for PARG interaction with PCNA. We identified the non-canonical PARG PIP-box spanning the K409 residue (D407-F414) as a *bona fide* PCNA interacting moiety, exhibiting similar *in vitro* binding properties to most of the described PIP-boxes (micromolar affinity, 1 PIP-box peptide bound per PCNA monomer, negative enthalpy) (39). Notwithstanding the non-canonical sequence of the PARG PIP-box in lacking Q as the first residue, it contains a canonical TD motif known to mediate high-affinity PCNA binding (15). Moreover, its PCNA binding mode resembles that of canonical PIP-boxes, which suggests that PARG PIP-box may represent a new intermediate type of PIP-box. The previously reported PARG PIP-box (Q76-W82) (13) does not bind PCNA *in vitro* and when mutated does not affect PARG–PCNA interaction *in vivo*.

Previous analyses of PIP-box motifs showed the hydrophobic mode of interaction with PCNA (43,44). Our X-ray structure of the PARG non-canonical PIP-box peptide bound to PCNA revealed that PARG K409 interacts with

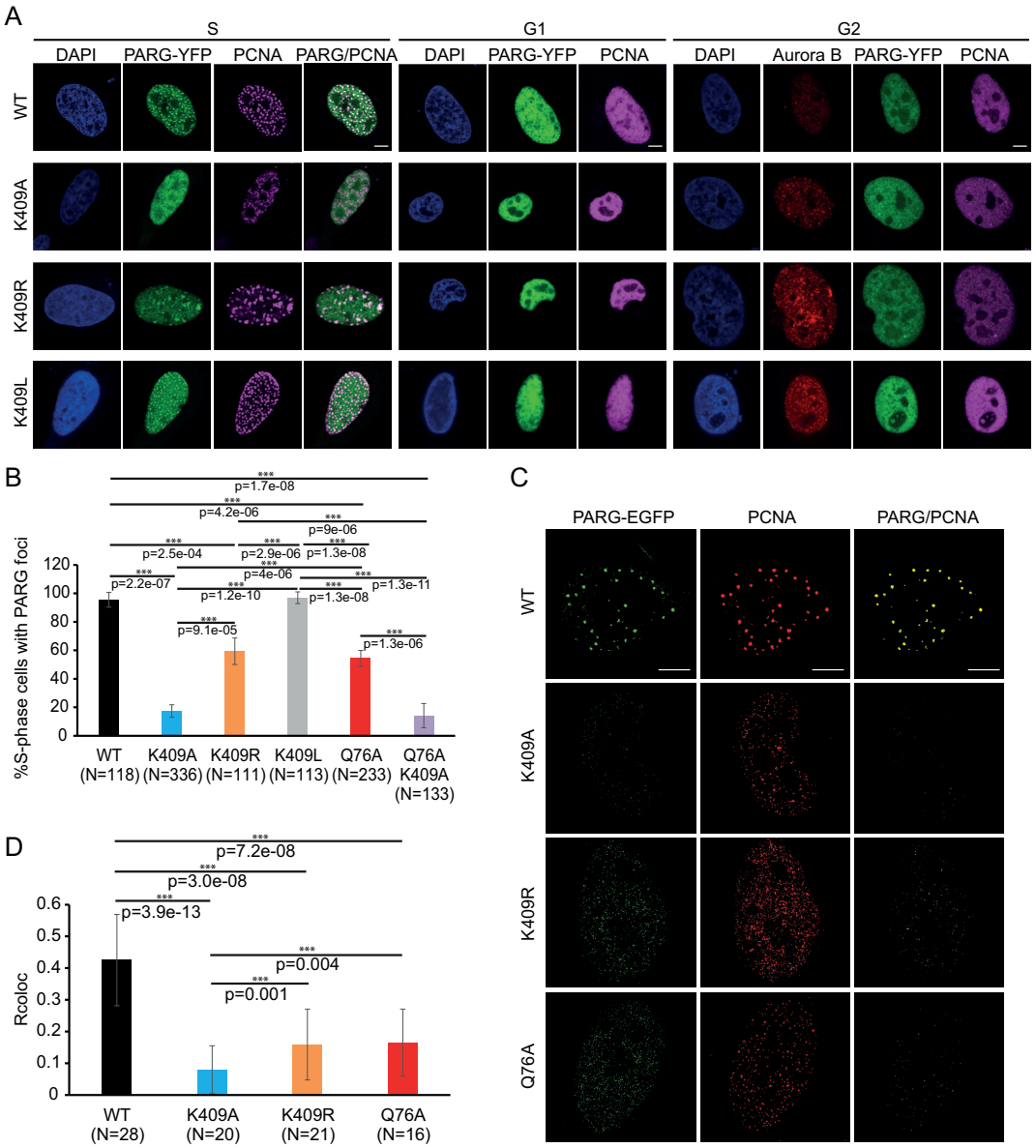

Figure 9. K409 mutation delocalizes PARG from PCNA-containing replication foci. (**A**) Immunofluorescence analysis of the localization of transiently transfected PARG-YFP wild-type and mutants throughout interphase. PCNA and Aurora B were used as markers of S phase and G2 phase, respectively. All PCNA and Aurora B images were adjusted with the same brightness/contrast settings. PARG-YFP images were differently adjusted to account for variable transfection levels. (**B**) The percentage of PARG mutants displaying punctate S-phase pattern. (**C**) 3D-SIM images of PARG–PCNA co-localization in S-phase U2OS cells. U2OS cells were transfected with PARG–EGFP wild-type, K409A, K409R and Q76A mutants and stained with anti-GFP and anti-PCNA. Representative images of co-localized pixels are shown. (**D**) Analysis of PARG–PCNA colocalization using Pearson colocalisation coefficient (Rcoloc). For Tetra spec beads Rcoloc = 0.9095 was calculated, while negative control without anti-PCNA staining gave Rcoloc = 0.005. Scale bars indicate 5 μm. Error bars represent sd. *P*-values were calculated using Student's *t*-test.

PCNA in a mixed hydrophobic/electrostatic mode. On the one hand, K409 stabilizes PARG–PCNA binding via hydrophobic interactions, as evidenced by the neutral effect of the K409L mutation. On the other hand, electrostatic interactions between the K409 ϵ-amino group and S43 within the hydrophilic PCNA region tune the interaction, depending on the acetylation state of the K409 ϵ-amino group: K409 acetylation reduces PARG–PCNA interaction by 2-fold *in vitro*. However, we were unable to test the effect of the K409 acetylation on PARG–PCNA interaction *in vivo*, as deacetylase inhibitors (trichostatin A and nicotinamide) and anacardic acid failed to affect PARG K409 acetylation levels (data not shown).

The degree of hydrophobic packing of PIP-box-containing peptides has been considered as the determinant of their binding affinity towards PCNA (37). However, it has remained unclear how PCNA-bound proteins cycle between bound and unbound states during the dynamic process of DNA replication (37). Our discovery of a mixed electrostatic/hydrophobic mode of PIP-box mediated interactions reflected in the PARG K409 residue may explain how PCNA-binding proteins switch between

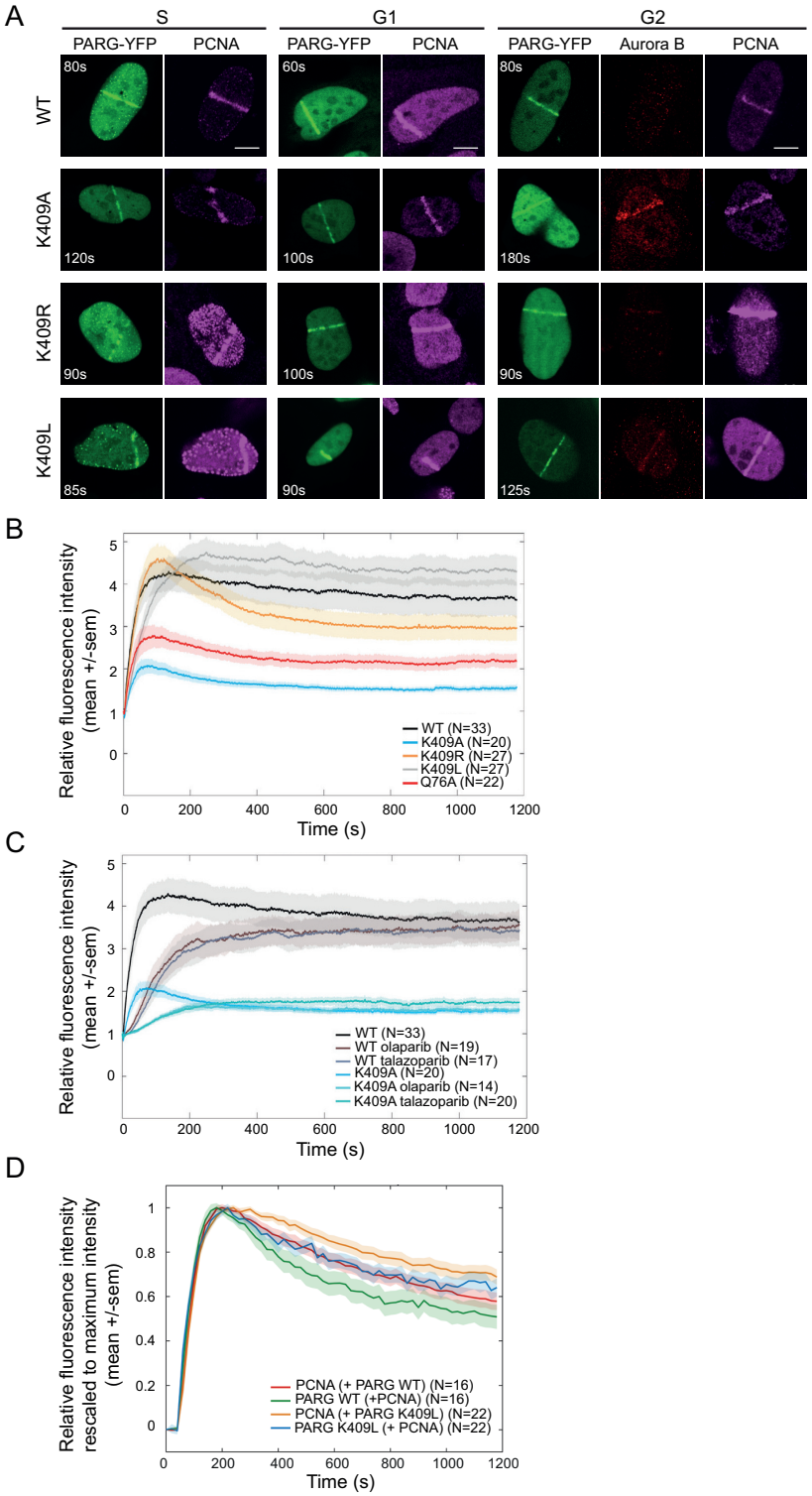

Figure 10. K409 mutations impair PARG recruitment to the sites of laser-induced DNA damage in U2OS cells. DNA damage was induced with a 355 nm pulsed laser as a line across the nucleus followed by live imaging analysis of the recruitment of PARG-YFP wild-type and mutants to the laser line. (**A**) Maximum recruitment live images of PARG-YFP wild-type and point mutants in different stages of the cell cycle. Cells were fixed at the point of maximum recruitment and stained with anti-PCNA and anti-Aurora B as markers of S-phase and G2 cells, respectively. Imperfect alignment of composite pictures stems from the difference in acquisition (live vs fixed). Scale bars indicate 5 μm. (B and C) Analysis of the recruitment kinetics of (**B**) wild-type PARG-YFP, Q76A and K409 mutants in G1/G2 cells by spinning disc microscopy and (**C**) wild-type PARG and K409A in the presence of PARP1/2 inhibitors olaparib (10 μM) and talazoparib (100 nM) applied for 1 h prior to imaging. (**D**) Simultaneous imaging of mRFP–PCNA and PARG–EGFP WT and K409L recruitment and dissociation from laser-induced DNA damage sites by split-view widefield microscopy. Relative fluorescence intensity was rescaled according to maximum recruitment in order to observe dissociation profiles. (**B-D**) Data from three independent experiments (mean ± SEM) are shown. The number of analysed cells is indicated in the plot legends.

weak and strong binding modes; the lysine residue in the non-canonical PARG PIP-box stabilizes PARG–PCNA interaction through its hydrophobic aliphatic chain while at the same time providing a transient switch via its positively charged and acetylatable amino group. The advantage of K409 over L409 in enabling transient modulation of PARG–PCNA interaction likely extends to translesion synthesis polymerases Pol κ and Pol ι that also have a lysine residue in their non-canonical PIP-box.

Studies of PCNA binding to fragments of intrinsically disordered p15 revealed interactions outside the canonical PIP-box that reach into the PCNA ring and contribute to the binding free energy (55). Such extended binding interface coupled to the dynamic binding of PARG to PCNA may explain the discrepancies between mutagenesis data using full-length PARG *in vivo* and PARG peptides *in vitro*. For example, PARG K409A mutant showed an almost complete loss of PCNA interaction in the context of a full-length protein *in vivo* (co-IP, FLIM-FRET), while *in vitro* interaction of the 19 aa-long PARG peptide with PCNA was reduced only 7.5 fold. The discrepancy between *in vivo* and *in vitro* interaction was also observed for PARG D412 and F414, whereby D412A mutation had a stronger effect *in vivo*, whereas F414 showed the opposite effect. PARG binding to PCNA in the context of a full-length protein is likely dynamic and modulated by residues outside of the PIP-box.

Collectively, our data provide comprehensive insights into the mechanism and regulation of PARG interaction with PCNA. We identified a non-canonical PIP-box within the disordered regulatory region of PARG as the interaction interface with PCNA and demonstrated that the K409 residue serves a stabilizing function via its hydrophobic side-chain and a transient fine-tuning function via its acetylatable amino group. The K409 residue emerged as the critical regulator of PARG localization within replication foci and PARG recruitment and dissociation from DNA damage sites.

ACCESSION NUMBERS

Atomic coordinates and structure factors for the reported crystal structure have been deposited with the Protein Data bank under accession number 5MAV.

SUPPLEMENTARY DATA

Supplementary Data are available at NAR Online.

ACKNOWLEDGEMENTS

We thank Susanne Opravil and Otto Hudecz for mass spectrometry analysis; Joachim Garbrecht for assistance with image analysis; Martin Puchinger for CD analysis; Mathias Madalinski for synthesizing PARG peptides; Dragana Ahel, Ivan Ahel, Andreas Brachner, Cristina Cardoso, Daniel Gerlich, Raul Mostoslavsky and Michael Potente for sharing materials; Thomas Schwarz for ITC advice; Graham Warren, Tim Skern and Matthias Schäfer for proofreading the manuscript.

FUNDING

MFPL start-up grant; Vienna Science and Technology Fund [LS14-001 to D.S.]; Austrian Science Fund Grant 'DK: Integrative Structural Biology' [W1258 to D.S.]; Austrian Federal Ministry of Science, Research & Economy and the City of Vienna through the Vienna Biocenter Core Facilities (to L.Z., K.E.); European Research Council Starting Independent grant [279408 to B.Z.]; University of Vienna financial support (to K.D.C.). Funding for open access charge: Vienna Science and Technology Fund [LS14-001].
Conflict of interest statement. None declared.

REFERENCES

1. Gibson,B.A. and Kraus,W.L. (2012) New insights into the molecular and cellular functions of poly(ADP-ribose) and PARPs. *Nat. Rev. Mol. Cell Biol.*, **13**, 411–424.
2. De Vos,M., Schreiber,V. and Dantzer,F. (2012) The diverse roles and clinical relevance of PARPs in DNA damage repair: current state of the art. *Biochem. Pharmacol.*, **84**, 137–146.
3. Beneke,S. (2012) Regulation of chromatin structure by poly(ADP-ribosyl)ation. *Front. Genet.*, **3**, 169.
4. Abplanalp,J. and Hottiger,M.O. (2016) Cell fate regulation by chromatin ADP-ribosylation. *Semin. Cell Dev. Biol.*, **63**, 114–122.
5. Tallis,M., Morra,R., Barkauskaite,E. and Ahel,I. (2014) Poly(ADP-ribosyl)ation in regulation of chromatin structure and the DNA damage response. *Chromosoma*, **123**, 79–90.
6. Alvarez-Gonzalez,R. and Althaus,F.R. (1989) Poly(ADP-ribose) catabolism in mammalian cells exposed to DNA-damaging agents. *Mutat. Res.*, **218**, 67–74.
7. Barkauskaite,E., Jankevicius,G. and Ahel,I. (2015) Structures and mechanisms of enzymes employed in the synthesis and degradation of PARP-dependent protein ADP-ribosylation. *Mol. Cell*, **58**, 935–946.
8. Meyer-Ficca,M.L., Meyer,R.G., Coyle,D.L., Jacobson,E.L. and Jacobson,M.K. (2004) Human poly(ADP-ribose) glycohydrolase is expressed in alternative splice variants yielding isoforms that localize to different cell compartments. *Exp. Cell Res.*, **297**, 521–532.
9. Barkauskaite,E., Jankevicius,G., Ladurner,A.G., Ahel,I. and Timinszky,G. (2013) The recognition and removal of cellular poly(ADP-ribose) signals. *FEBS J.*, **280**, 3491–3507.
10. Slade,D., Dunstan,M.S., Barkauskaite,E., Weston,R., Lafite,P., Dixon,N., Ahel,M., Leys,D. and Ahel,I. (2011) The structure and catalytic mechanism of a poly(ADP-ribose) glycohydrolase. *Nature*, **477**, 616–620.
11. Kim,I.K., Kiefer,J.R., Ho,C.M., Stegeman,R.A., Classen,S., Tainer,J.A. and Ellenberger,T. (2012) Structure of mammalian poly(ADP-ribose) glycohydrolase reveals a flexible tyrosine clasp as a substrate-binding element. *Nat. Struct. Mol. Biol.*, **19**, 653–656.
12. Barkauskaite,E., Brassington,A., Tan,E.S., Warwicker,J., Dunstan,M.S., Banos,B., Lafite,P., Ahel,M., Mitchison,T.J., Ahel,I. *et al.* (2013) Visualization of poly(ADP-ribose) bound to PARG reveals inherent balance between exo- and endo-glycohydrolase activities. *Nat. Commun.*, **4**, 2164.
13. Mortusewicz,O., Fouquerel,E., Ame,J.C., Leonhardt,H. and Schreiber,V. (2011) PARG is recruited to DNA damage sites through poly(ADP-ribose)- and PCNA-dependent mechanisms. *Nucleic Acids Res.*, **39**, 5045–5056.
14. Warbrick,E. (1998) PCNA binding through a conserved motif. *BioEssays*, **20**, 195–199.
15. Choe,K.N. and Moldovan,G.L. (2017) Forging ahead through darkness: PCNA, still the principal conductor at the replication fork. *Mol. Cell*, **65**, 380–392.
16. Ame,J.C., Fouquerel,E., Gauthier,L.R., Biard,D., Boussin,F.D., Dantzer,F., de Murcia,G. and Schreiber,V. (2009) Radiation-induced mitotic catastrophe in PARG-deficient cells. *J. Cell Sci.*, **122**, 1990–2002.
17. Li,C., Wen,A., Shen,B., Lu,J., Huang,Y. and Chang,Y. (2011) FastCloning: a highly simplified, purification-free, sequence- and ligation-independent PCR cloning method. *BMC Biotechnol.*, **11**, 92.
18. Sporbert,A., Domaing,P., Leonhardt,H. and Cardoso,M.C. (2005) PCNA acts as a stationary loading platform for transiently

interacting Okazaki fragment maturation proteins. *Nucleic Acids Res.*, **33**, 3521–3528.
19. Kall,L., Canterbury,J.D., Weston,J., Noble,W.S. and MacCoss,M.J. (2007) Semi-supervised learning for peptide identification from shotgun proteomics datasets. *Nat. Methods*, **4**, 923–925.
20. Taus,T., Kocher,T., Pichler,P., Paschke,C., Schmidt,A., Henrich,C. and Mechtler,K. (2011) Universal and confident phosphorylation site localization using phosphoRS. *J. Proteome Res.*, **10**, 5354–5362.
21. Kabsch,W. (2010) XDS. *Acta Crystallogr. D, Biol. Crystallogr.*, **66**, 125–132.
22. Winn,M.D., Ballard,C.C., Cowtan,K.D., Dodson,E.J., Emsley,P., Evans,P.R., Keegan,R.M., Krissinel,E.B., Leslie,A.G., McCoy,A. *et al.* (2011) Overview of the CCP4 suite and current developments. *Acta Crystallogr. D, Biol. Crystallogr.*, **67**, 235–242.
23. McCoy,A.J., Grosse-Kunstleve,R.W., Adams,P.D., Winn,M.D., Storoni,L.C. and Read,R.J. (2007) Phaser crystallographic software. *J. Appl. Crystallogr.*, **40**, 658–674.
24. Murshudov,G.N., Vagin,A.A. and Dodson,E.J. (1997) Refinement of macromolecular structures by the maximum-likelihood method. *Acta Crystallogr. D, Biol. Crystallogr.*, **53**, 240–255.
25. Adams,P.D., Afonine,P.V., Bunkoczi,G., Chen,V.B., Davis,I.W., Echols,N., Headd,J.J., Hung,L.W., Kapral,G.J., Grosse-Kunstleve,R.W. *et al.* (2010) PHENIX: a comprehensive Python-based system for macromolecular structure solution. *Acta Crystallogr. D, Biol. Crystallogr.*, **66**, 213–221.
26. Emsley,P. and Cowtan,K. (2004) Coot: model-building tools for molecular graphics. *Acta Crystallogr. D, Biol. Crystallogr.*, **60**, 2126–2132.
27. Dolinsky,T.J., Czodrowski,P., Li,H., Nielsen,J.E., Jensen,J.H., Klebe,G. and Baker,N.A. (2007) PDB2PQR: expanding and upgrading automated preparation of biomolecular structures for molecular simulations. *Nucleic Acids Res.*, **35**, W522–W525.
28. Pronk,S., Pall,S., Schulz,R., Larsson,P., Bjelkmar,P., Apostolov,R., Shirts,M.R., Smith,J.C., Kasson,P.M., van der Spoel,D. *et al.* (2013) GROMACS 4.5: a high-throughput and highly parallel open source molecular simulation toolkit. *Bioinformatics (Oxford, England)*, **29**, 845–854.
29. Lindorff-Larsen,K., Piana,S., Palmo,K., Maragakis,P., Klepeis,J.L., Dror,R.O. and Shaw,D.E. (2010) Improved side-chain torsion potentials for the Amber ff99SB protein force field. *Proteins*, **78**, 1950–1958.
30. Jorgensen,W.L. and Madura,J.D. (1983) Solvation and conformation of methanol in water. *J. Am. Chem. Soc.*, **105**, 1407–1413.
31. Hoover,W.G. (1985) Canonical dynamics: equilibrium phase-space distributions. *Phys. Rev. A*, **31**, 1695–1697.
32. Parrinello,M. and Rahman,A. (1981) Polymorphic transitions in single crystals: a new molecular dynamics method. *J. Appl. Phys.*, **52**, 9.
33. Hess,B., Bekker,H., Berendsen,H. and Fraaije,J. (1997) 3 LINCS: a linear constraint solver for molecular simulations. *J. Comput. Chem.*, **18**, 10.
34. Humphrey,W., Dalke,A. and Schulten,K. (1996) VMD: visual molecular dynamics. *J. Mol. Graph.*, **14**, 27–38.
35. Pyrkov,T.V., Chugunov,A.O., Krylov,N.A., Nolde,D.E. and Efremov,R.G. (2009) PLATINUM: a web tool for analysis of hydrophobic/hydrophilic organization of biomolecular complexes. *Bioinformatics (Oxford, England)*, **25**, 1201–1202.
36. Schrodinger, LLC (2015) https://www.schrodinger.com/.
37. Mailand,N., Gibbs-Seymour,I. and Bekker-Jensen,S. (2013) Regulation of PCNA-protein interactions for genome stability. *Nat. Rev. Mol. Cell Biol.*, **14**, 269–282.
38. Hishiki,A., Hashimoto,H., Hanafusa,T., Kamei,K., Ohashi,E., Shimizu,T., Ohmori,H. and Sato,M. (2009) Structural basis for novel interactions between human translesion synthesis polymerases and proliferating cell nuclear antigen. *J. Biol. Chem.*, **284**, 10552–10560.
39. Bruning,J.B. and Shamoo,Y. (2004) Structural and thermodynamic analysis of human PCNA with peptides derived from DNA polymerase-delta p66 subunit and flap endonuclease-1. *Structure*, **12**, 2209–2219.
40. Havens,C.G. and Walter,J.C. (2009) Docking of a specialized PIP Box onto chromatin-bound PCNA creates a degron for the ubiquitin ligase CRL4Cdt2. *Mol. Cell*, **35**, 93–104.
41. Broussard,J.A., Rappaz,B., Webb,D.J. and Brown,C.M. (2013) Fluorescence resonance energy transfer microscopy as demonstrated by measuring the activation of the serine/threonine kinase Akt. *Nat. Protoc.*, **8**, 265–281.
42. Zondlo,N.J. (2013) Aromatic-proline interactions: electronically tunable CH/pi interactions. *Acc. Chem. Res.*, **46**, 1039–1049.
43. Haracska,L., Acharya,N., Unk,I., Johnson,R.E., Hurwitz,J., Prakash,L. and Prakash,S. (2005) A single domain in human DNA polymerase iota mediates interaction with PCNA: implications for translesion DNA synthesis. *Mol. Cell. Biol.*, **25**, 1183–1190.
44. Ogi,T., Kannouche,P. and Lehmann,A.R. (2005) Localisation of human Y-family DNA polymerase kappa: relationship to PCNA foci. *J. Cell Sci.*, **118**, 129–136.
45. Gulbis,J.M., Kelman,Z., Hurwitz,J., O'Donnell,M. and Kuriyan,J. (1996) Structure of the C-terminal region of p21(WAF1/CIP1) complexed with human PCNA. *Cell*, **87**, 297–306.
46. Gsponer,J. and Babu,M.M. (2009) The rules of disorder or why disorder rules. *Progr. Biophys. Mol. Biol.*, **99**, 94–103.
47. Wright,P.E. and Dyson,H.J. (2015) Intrinsically disordered proteins in cellular signalling and regulation. *Nat. Rev. Mol. Cell Biol.*, **16**, 18–29.
48. Vidal,A.E., Kannouche,P., Podust,V.N., Yang,W., Lehmann,A.R. and Woodgate,R. (2004) Proliferating cell nuclear antigen-dependent coordination of the biological functions of human DNA polymerase iota. *J. Biol. Chem.*, **279**, 48360–48368.
49. Bienko,M., Green,C.M., Crosetto,N., Rudolf,F., Zapart,G., Coull,B., Kannouche,P., Wider,G., Peter,M., Lehmann,A.R. *et al.* (2005) Ubiquitin-binding domains in Y-family polymerases regulate translesion synthesis. *Science (New York, N.Y.)*, **310**, 1821–1824.
50. Menear,K.A., Adcock,C., Boulter,R., Cockcroft,X.L., Copsey,L., Cranston,A., Dillon,K.J., Drzewiecki,J., Garman,S., Gomez,S. *et al.* (2008) 4-[3-(4-cyclopropanecarbonylpiperazine-1-carbonyl)-4-fluorobenzyl]-2H-phthalazin- 1-one: a novel bioavailable inhibitor of poly(ADP-ribose) polymerase-1. *J. Med. Chem.*, **51**, 6581–6591.
51. Shen,Y., Rehman,F.L., Feng,Y., Boshuizen,J., Bajrami,I., Elliott,R., Wang,B., Lord,C.J., Post,L.E. and Ashworth,A. (2013) BMN 673, a novel and highly potent PARP1/2 inhibitor for the treatment of human cancers with DNA repair deficiency. *Clin. Cancer Res.*, **19**, 5003–5015.
52. Mortusewicz,O., Fouquerel,E., Ame,J.C., Leonhardt,H. and Schreiber,V. (2011) PARG is recruited to DNA damage sites through poly(ADP-ribose)- and PCNA-dependent mechanisms. *Nucleic Acids Res.*, **39**, 5045–5056.
53. Hatakeyama,K., Nemoto,Y., Ueda,K. and Hayaishi,O. (1986) Purification and characterization of poly(ADP-ribose) glycohydrolase. Different modes of action on large and small poly(ADP-ribose). *J. Biol. Chem.*, **261**, 14902–14911.
54. Choudhary,C., Weinert,B.T., Nishida,Y., Verdin,E. and Mann,M. (2014) The growing landscape of lysine acetylation links metabolism and cell signalling. *Nat. Rev. Mol. Cell. Biol.*, **15**, 536–550.
55. De Biasio,A., de Opakua,A.I., Mortuza,G.B., Molina,R., Cordeiro,T.N., Castillo,F., Villate,M., Merino,N., Delgado,S., Gil-Carton,D. *et al.* (2015) Structure of p15(PAF)-PCNA complex and implications for clamp sliding during DNA replication and repair. *Nat. Commun.*, **6**, 6439.